



Low temperature oxidation of diesel soot particles over one-dimensional 2 × 3 tunnel-structured $\text{Na}_2\text{Mn}_5\text{O}_{10}$ catalysts

Di Yu ^{a,b}, Chao Peng ^a, Yu Ren ^a, Lanyi Wang ^a, Chunlei Zhang ^b, Xiaoqiang Fan ^a, Xuehua Yu ^{a,*}, Zhen Zhao ^{a,b,**}

^a Institute of Catalysis for Energy and Environment, College of Chemistry and Chemical Engineering, Shenyang Normal University, Shenyang, Liaoning 110034, China

^b State Key Laboratory of Heavy Oil Processing, China University of Petroleum, 18# Fuxue Road, Chang Ping, Beijing 102249, China



ARTICLE INFO

Keywords:
 $\text{Na}_2\text{Mn}_5\text{O}_{10}$ phase oxide
 Tunnel Structure
 Catalysts
 Low temperature
 Soot oxidation

ABSTRACT

Tunnel-structured manganese oxides have drawn widespread research attention due to their excellent oxidation properties for the soot oxidation reaction. In this study, a series of romanechite $\text{Na}_2\text{Mn}_5\text{O}_{10}$ catalysts with a 2 × 3 tunnel structure were synthesized via a facile hydrothermal method. The as-synthesized catalysts were investigated using X-ray diffraction, scanning and transmission electron microscopy, H_2 and soot temperature-programmed reduction, O_2 temperature-programmed desorption, NO temperature-programmed oxidation, X-ray photoelectron spectroscopy, and other measurements. Among all the catalysts, the $\text{Na}_1\text{Mn}_9\text{O}_{12}$ catalyst exhibited the best catalytic performance for soot combustion, with T_{10} , T_{50} , and T_{90} values of 281 °C, 317 °C, and 343 °C, respectively, which were considerably reduced to 271 °C, 310 °C, and 335 °C in the existence of 10% H_2O . The results of multiple characterization methods indicated that the $\text{Na}_2\text{Mn}_5\text{O}_{10}$ catalysts exhibit good reducibility, strong oxygen adsorption and activation capacity, and NO to NO_2 oxidation ability. Moreover, the active sites (Mn and oxygen vacancies) and reaction mechanism (Langmuir–Hinshelwood) were also revealed by in-situ DRIFT and density functional theory calculations results. This study details a new strategy for the design and synthesis of efficient soot oxidation catalysts with practical application prospects.

1. Introduction

Diesel engines are widely applied in the transportation, machinery, and agricultural industries due to their high efficiency, good economy, strong durability, and low content of unburned hydrocarbons [1–3]. However, soot particles emitted by diesel engines pose a severe threat to the environment and human health, as they are one of the main contributors to atmospheric fine particulate matter (PM_{2.5}) in the urban air [4,5]. Therefore, in the purification of diesel engine exhaust, the elimination of soot particles is an important task that has significant practical and environmental significance. To date, the combination of diesel particulate filters (DPFs) and catalysts has been considered to be one of the most efficient after-treatment techniques for exhaust gases, the catalytic behavior of which is heavily dependent on the performance of the coated catalysts employed [6,7]. In recent decades, numerous catalytic materials have been investigated and applied for the soot

oxidation reaction, among which noble metal-containing catalysts have been revealed to be the most suitable candidates due to their excellent oxidation performance. However, the cost-effectiveness and scarcity of noble-metal catalysts greatly restrict their commercial prospects; therefore, research is heavily focused on developing cheaper alternatives.

To this aim, manganese oxides (MnO_x) not only have diverse structures, are environmentally compatible, and low cost, but they also have unique redox properties ($\text{Mn}^{2+}/\text{Mn}^{3+}$ or $\text{Mn}^{3+}/\text{Mn}^{4+}$ facile redox cycle) [8,9]. Meanwhile, it has been reported that MnO_x materials with a tunnel structure (microporous structure) possess excellent soot oxidation properties [10]. Alkali metals with a low melting point, high fluidity, and strong electron-donating ability are also beneficial for improving the contact efficiency and intrinsic activity of catalysts for soot combustion [11,12]. Therefore, introducing alkali metal ions (Li, Na, K, Rb, and Cs) into the tunnel-structured MnO_x materials effectively

* Corresponding author.

** Corresponding author at: Institute of Catalysis for Energy and Environment, College of Chemistry and Chemical Engineering, Shenyang Normal University, Shenyang, Liaoning 110034, China.

E-mail addresses: yuxuehua1986@163.com (X. Yu), zhaozhen1586@163.com, zhenzhao@cup.edu.cn (Z. Zhao).

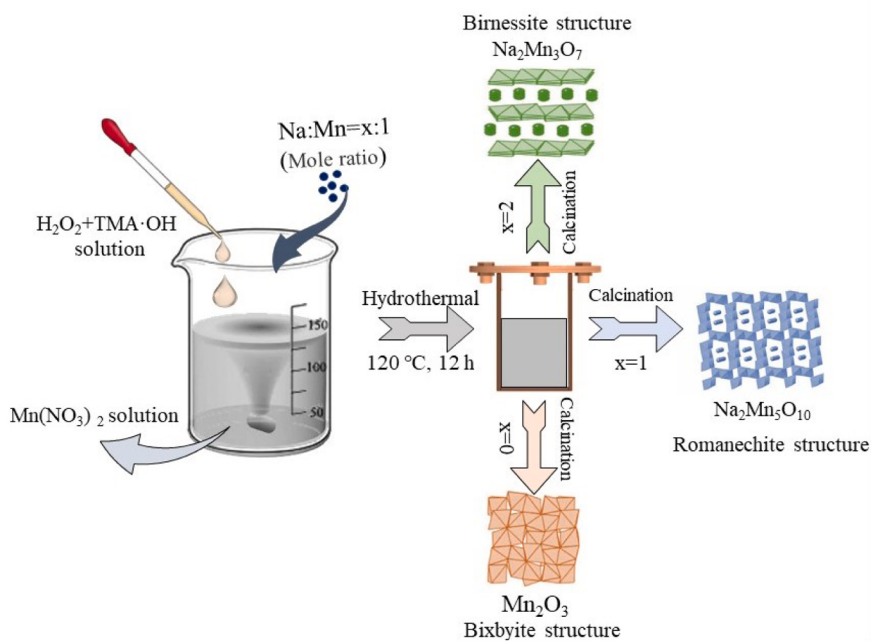


Fig. 1. A schematic diagram describing the synthesis of $\text{Na}_x\text{Mn}_y\text{O}_8$ catalysts.

enhances the catalytic performance of soot-oxidation catalysts. More importantly, the introduction of alkali metal ions into the tunnel structure of MnO_x can stabilize their skeletons, improving the activity of the catalysts while ensuring their stability [13]. As is well known, the catalytic combustion of soot is a heterogeneous catalytic reaction that occurs at a three-phase (gas ($\text{O}_2/\text{NO}/\text{NO}_2$)-solid (catalyst)-solid (soot)) contact interface [14]. Aside from the contact efficiency and intrinsic activity of the catalyst, the capacity of micropores in tunnel-structured catalysts to adsorb and activate small gas molecules is also a critical factor in optimizing the catalytic performance of catalysts. In our previous studies, monoclinic-structured (I4/m) cryptomelane ($\text{K}_{2-x}\text{Mn}_8\text{O}_{16}$) with edge-sharing double 2×2 octahedral MnO_6 chains, some of which are corner-sharing to form one-dimensional tunnels of 0.46 nm in size, was shown to exhibit excellent catalytic performance [15,16]. However, $\text{Na}_2\text{Mn}_5\text{O}_{10}$ catalysts have a tunnel structure that is three MnO_6 octahedra long and two octahedra wide (2×3 tunnel structure), which has rarely been reported in the field of soot combustion. In this study, a series of tunnel-structures romanechite-type $\text{Na}_2\text{Mn}_5\text{O}_{10}$ materials were successfully designed and prepared via a hydrothermal method. Moreover, multiple characterizations were conducted to comprehensively investigate the physical and chemical properties of the catalysts. Based on the detailed characterization results and density functional theory (DFT) calculations, a reaction mechanism was proposed for soot combustion over the $\text{Na}_2\text{Mn}_5\text{O}_{10}$ catalysts, which is discussed herein. Moreover, the catalytic performance, water and sulfur resistance, and stability of the catalysts were also investigated to further identify the characteristics of romanechite-type $\text{Na}_2\text{Mn}_5\text{O}_{10}$ for catalyzing soot combustion under various reaction conditions.

2. Experimental section

2.1. Catalyst preparation

The chemical reagents in this work are mainly tetramethylammonium hydroxide solution (TMA-OH, 25 wt%), hydrogen peroxide solution (H_2O_2 , 30 wt%), sodium nitrate (NaNO_3 , 99%) and manganese nitrate ($\text{Mn}(\text{NO}_3)_2$, 50 wt%). All chemicals (AR grades) were purchased from Sinopharm and were used as received without further purification. The deionized water (18.25 MΩ cm) was used for all the experiments.

The $\text{Na}_2\text{Mn}_5\text{O}_{10}$ catalysts were synthesized via a hydrothermal method, the detailed preparation process of which is shown in Fig. 1. In brief, 4.75 g of $\text{Mn}(\text{NO}_3)_2$ was dissolved in 40 mL of deionized water. Then, 6.9 mL of 30% H_2O_2 , and 17.2 mL of 25% TMA-OH were mixed and diluted with deionized water to obtain an 80 mL solution mixture, which was added to the aqueous solution of $\text{Mn}(\text{NO}_3)_2$ under magnetic stirring. Subsequently, 1.128 g of NaNO_3 was added to the above solution, followed by continuous stirring for 5 min. The mixture was then transferred to a 150 mL Teflon-lined autoclave and was hydrothermally treated at 120 °C for 12 h. After the autoclave was cooled to room temperature, the resultant products were separated by filtration and dried at 80 °C overnight. Finally, the $\text{Na}_2\text{Mn}_5\text{O}_{10}$ catalysts were obtained after calcination at 550 °C for 3 h under an air atmosphere. The as-prepared catalysts were named $\text{Na}_x\text{Mn}_y\text{O}_8\text{-T}$ for simplicity, where x is the molar ratio of NaNO_3 to $\text{Mn}(\text{NO}_3)_2$, and T is the hydrothermal reaction temperature. The methods for synthesizing catalysts with different molar ratios of Na to Mn and the hydrothermal reaction temperatures are listed in Table S1.

2.2. Physical and chemical characterizations

The as-prepared $\text{Na}_x\text{Mn}_y\text{O}_8$ catalysts were determined for their phase structures using X-ray powder diffraction (Ultima IV, Rigaku), and the XRD patterns were recorded within the 2θ range of 10–90° at a scanning rate of 10 °/min. Raman spectra were recorded on a HORIBA LabRAM HR Evolution spectrometer with a 532-nm laser in the 100–1200 cm^{-1} range. The morphologies were obtained by scanning electron microscopy (SEM, Hitachi SU8010N) and transmission electron microscopy (TEM, JEO1 JEM LaB6 2100). The BET specific surface areas of catalysts were characterized by a TriStar II: 3020 Micromeritics analyzer. The X-ray photoelectron spectra were acquired on a Thermo ESCALAB 250Xi spectrometer to characterize the surface chemical compositions and chemical states of samples. H_2 temperature-programmed reduction ($\text{H}_2\text{-TPR}$) and O_2 temperature-programmed desorption ($\text{O}_2\text{-TPD}$) were carried on a TP-5076 chemisorption instrument with a thermal conductivity detector. For the $\text{H}_2\text{-TPR}$ experiments, 50 mg of sample was pretreated in N_2 at 300 °C for 1 h, and the flow was changed to 10% H_2/N_2 (50 mL/min) after cooling to 50 °C. The temperature was gradually increased to 800 °C at a rate of 10 °C/min, and the hydrogen

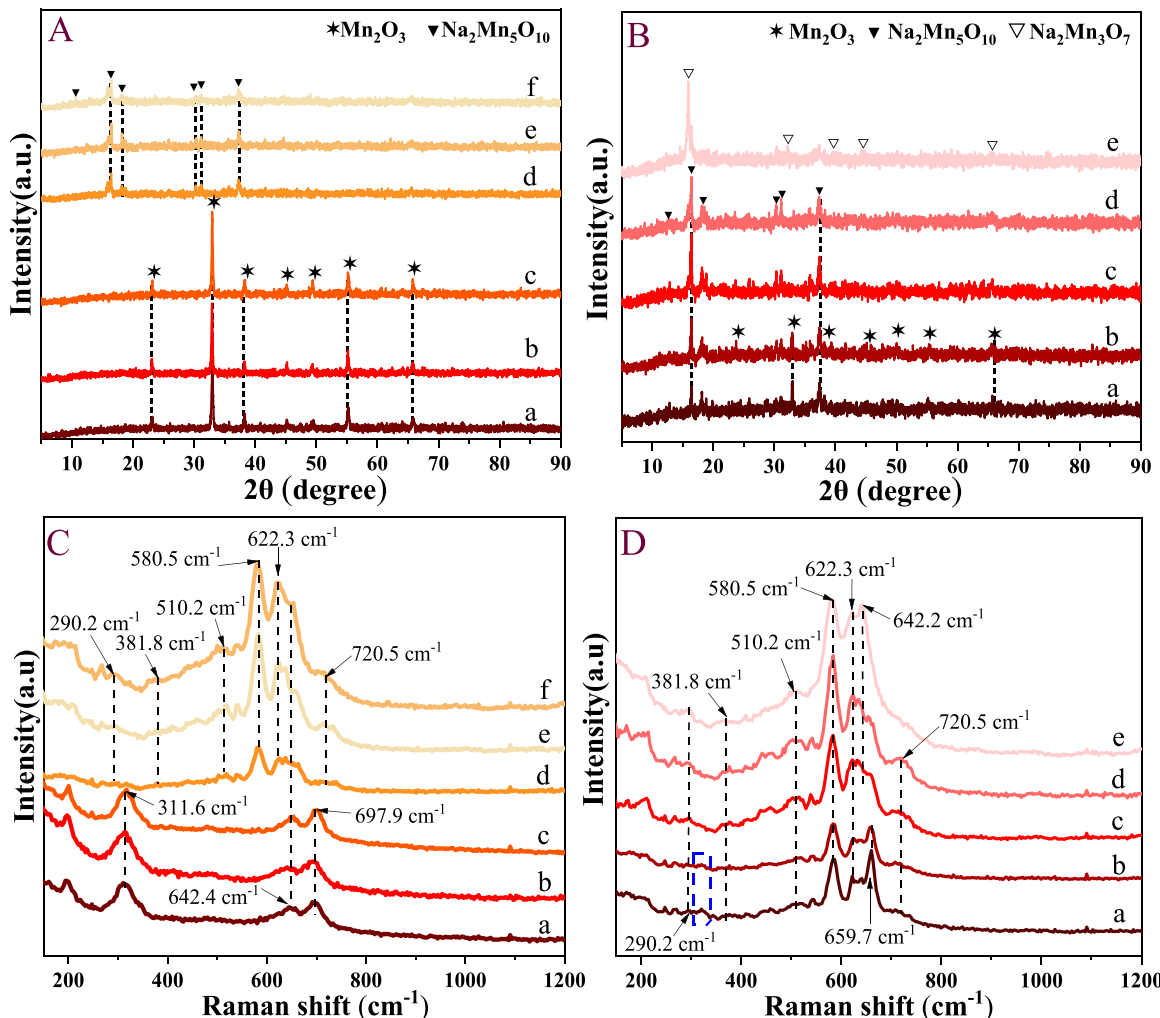


Fig. 2. X-ray diffraction patterns (A, B) and Raman spectra (C, D) of as-prepared $\text{Na}_x\text{Mn}_y\text{O}_8$ catalysts with different hydrothermal reaction temperature and Na/Mn molar ratio (A, C: a: $\text{Na}_0\text{Mn}_y\text{O}_8$ -20; b: $\text{Na}_0\text{Mn}_y\text{O}_8$ -80; c: $\text{Na}_0\text{Mn}_y\text{O}_8$ -120; d: $\text{Na}_1\text{Mn}_y\text{O}_8$ -20; e: $\text{Na}_1\text{Mn}_y\text{O}_8$ -80; f: $\text{Na}_1\text{Mn}_y\text{O}_8$ -120; B, D: a: $\text{Na}_{0.25}\text{Mn}_y\text{O}_8$ -120; b: $\text{Na}_{0.5}\text{Mn}_y\text{O}_8$ -120; c: $\text{Na}_{0.75}\text{Mn}_y\text{O}_8$ -120; d: $\text{Na}_{1.5}\text{Mn}_y\text{O}_8$ -120; e: $\text{Na}_2\text{Mn}_y\text{O}_8$ -120).

consumption of samples were calibrated with CuO . For the O_2 -TPD experiments, 100 mg of sample was pretreated in air at 300 °C for 1 h. When the temperature dropped to 50 °C, it was exposed under an oxygen atmosphere to form adsorbed oxygen species. Subsequently, the flow gas was switched to He (50 mL/min), and the temperature was raised to 900 °C at 10 °C/min. Soot temperature-programmed reduction (soot-TPR) were performed on a gas chromatograph (Agilent 7890B). A loose contact mixture of 100 mg catalyst and 10 mg soot was processed in Ar (50 mL/min) at 200 °C for 30 min, and then heated from 200 °C to 800 °C at a rate of 10 °C/min. NO temperature-programmed oxidation (NO-TPO) were examined by an nCLD 62 NOx Analyzer. The catalysts were pretreated at 200 °C in Ar for 30 min, and then heated from 100 °C to 600 °C in a gas mixture containing 10% O_2 , 1000 ppm NO and Ar at a flow rate of 50 mL/min at a rate of 2 °C/min. In situ diffuse reflection infrared fourier transform spectroscopy (In situ DRIFTS) were performed on a Vertex 80 v spectrometer (Bruker).

All spin-polarized DFT calculations were performed as implemented in the Vienna ab initio simulation package (VASP) [17,18]. The Perdew-Burke-Ernzerhof functional within the generalized gradient approximation (GGA-PBE) was utilized to describe the electron exchange-correlation effect [19]. The core-valence electron interaction was described by the projector augmented wave (PAW) pseudopotential [20]. The plane-wave basis set with an energy cutoff of 450 eV was used in the calculations. For all the geometric optimization, the conjugate

gradient algorithm was used in ionic optimization, and the convergence thresholds in electronic relaxation and Hellmann-Feynman force on each atom were set to 10^{-5} eV and 0.02 eV/Å, respectively. The DFT + U approach was applied to the Mn 3d state with $\text{U}_{\text{eff}} = 1.6$ eV to correct the self-interaction error inherent in DFT calculation [21]. The DFT-D3 method with Becke Jonson damping is applied owing to the consideration of long-range van der Waals (vdW) interactions [22,23]. The Brillouin zone was sampled using the Monkhorst-Pack scheme with $3 \times 3 \times 1$ k-meshes [24]. Adsorption energies have been calculated using $E_{\text{ad}} = E_{\text{tot}} - E_{\text{slab}} - E_X$, where E_{tot} is the total energy of the catalysts with the adsorbate X, E_{slab} is the energy of slab, and E_X is the energy of the adsorbate in the gas phase. According to this definition, exothermic adsorption results in a negative value.

2.3. Catalytic performance tests

The catalytic activities of as-prepared catalysts were evaluated by temperature-programmed oxidation (TPO) measurements. In each TPO experiment, the reaction temperature was raised from 100 to 600 °C at a rate of 2 °C/min. Printex-U (25 nm diameter, Degussa) was used as model soot, consisting of 92.0% C, 0.7% H, 3.5% O, 0.1% N, 0.2% S, and 3.5% of other elements. 100 mg of catalyst and 10 mg of soot particles were mixed with a spatula to obtain loose contact mixture, and then the mixture was placed in the fixed-bed tubular quartz reactor ($\Phi = 8$ mm).

Table 1Crystalline phases and textural properties of as-prepared $\text{Na}_x\text{Mn}_y\text{O}_8$ catalysts.

Catalyst	Crystalline phase	Surface area (m^2/g) ^a	Pore size (nm) ^b	Total pore volume (cm^3/g) ^c	Crystalline sizes/ (nm) ^d
$\text{Na}_0\text{Mn}_y\text{O}_8\text{-}20$	Mn_2O_3	19.6	39.5	0.184	22.8
$\text{Na}_0\text{Mn}_y\text{O}_8\text{-}80$	Mn_2O_3	15.4	20.5	0.074	26.3
$\text{Na}_0\text{Mn}_y\text{O}_8\text{-}120$	Mn_2O_3	13.1	14.7	0.038	30.8
$\text{Na}_1\text{Mn}_y\text{O}_8\text{-}20$	$\text{Na}_2\text{Mn}_5\text{O}_{10}$	5.8	33.7	0.032	22.7
$\text{Na}_1\text{Mn}_y\text{O}_8\text{-}80$	$\text{Na}_2\text{Mn}_5\text{O}_{10}$	9.0	24.7	0.044	19.5
$\text{Na}_1\text{Mn}_y\text{O}_8\text{-}120$	$\text{Na}_2\text{Mn}_5\text{O}_{10}$	9.2	12.7	0.021	12.9
$\text{Na}_{0.25}\text{Mn}_y\text{O}_8\text{-}120$	$\text{Na}_2\text{Mn}_5\text{O}_{10} + \text{Mn}_2\text{O}_3$	5.8	18.4	0.017	23.3
$\text{Na}_{0.5}\text{Mn}_y\text{O}_8\text{-}120$	$\text{Na}_2\text{Mn}_5\text{O}_{10} + \text{Mn}_2\text{O}_3$	7.3	15.4	0.022	21.3
$\text{Na}_{0.75}\text{Mn}_y\text{O}_8\text{-}120$	$\text{Na}_2\text{Mn}_5\text{O}_{10}$	8.1	16.6	0.024	20.2
$\text{Na}_{1.5}\text{Mn}_y\text{O}_8\text{-}120$	$\text{Na}_2\text{Mn}_5\text{O}_{10}$	9.8	16.3	0.037	19.3
$\text{Na}_2\text{Mn}_y\text{O}_8\text{-}120$	$\text{Na}_2\text{Mn}_3\text{O}_7$	11.7	20.6	0.050	13.2

^a Calculated by BET method.^b Calculated by BJH adsorption average pore diameter.^c Calculated by BJH adsorption cumulative volume of pores between 1.7 nm and 300 nm diameter.^d Calculated by Scherer equation.

The soot combustion reaction occurs in a mixture gas containing 10% O_2 and 2000 ppm NO balanced with Ar with a flow rate of 50 mL/min. The outlet gas compositions were analyzed by an on-line Agilent 7890B gas chromatograph with a flame ionization detector (FID). The catalytic activities were estimated from the values of T_{10} , T_{50} , and T_{90} , defined as the temperatures corresponding to soot conversion rates of 10%, 50%, and 90%, respectively. The selectivity to CO_2 formation (S_{CO_2}) was defined as the ratio of CO_2 outlet concentration (C_{CO_2}) to the sum of CO_2 and CO outlet concentrations, i.e., $S_{\text{CO}_2} = C_{\text{CO}_2}/(C_{\text{CO}} + C_{\text{CO}_2})$. $S_{\text{CO}_2}^m$ denoted the S_{CO_2} value at the maximum temperature (T_m) corresponding to the highest soot combustion rate soot-burnt rate. The stability, water and sulfur resistance, and the activity under different NO concentrations were also measured to investigate the catalytic performance of as-prepared catalysts.

3. Results and discussion

3.1. Structural properties

As structure has a critical impact on catalytic performance, the structural properties of the as-prepared $\text{Na}_x\text{Mn}_y\text{O}_8$ catalysts were investigated using XRD and Raman spectroscopy. Fig. 2 shows the XRD patterns and Raman spectra of $\text{Na}_x\text{Mn}_y\text{O}_8$ catalysts prepared at different reaction temperatures with various Na:Mn molar ratios. As shown in Fig. 2Aa, for the $\text{Na}_0\text{Mn}_y\text{O}_8\text{-}20$ catalyst, the diffraction peaks located at around 23.1°, 32.9°, 38.2°, 45.2°, 49.3°, 55.1°, and 65.8° can be ascribed to the (211), (222), (400), (332), (134), (440), and (622) planes of the bixbyite Mn_2O_3 phase (space group: Ia/3, $a = b = c = 9.408 \text{ \AA}$, marked as *, JCPDS Card No. 65-7467) [25]. With an increase in the hydrothermal reaction temperature, the positions of diffraction peaks of the $\text{Na}_0\text{Mn}_y\text{O}_8\text{-}80$ and $\text{Na}_0\text{Mn}_y\text{O}_8\text{-}120$ catalysts remain consistent (Fig. 2Ab, c), while the changes in their intensity indicate that there may be differences in the grain size of the catalysts. In addition, introducing NaNO_3 under the same hydrothermal reaction conditions led to a drastic transformation in the crystal phase of the catalysts. As shown in Fig. 2Ad-f, the diffraction peaks of the $\text{Na}_1\text{Mn}_y\text{O}_8\text{-}20$, $\text{Na}_1\text{Mn}_y\text{O}_8\text{-}80$, and $\text{Na}_1\text{Mn}_y\text{O}_8\text{-}120$ catalysts, which are located at 2θ angles of 8.8° (001), 16.4° (201), 18.2° (002), 30.4° (−402), 31.2° (010), and 37.3° (112), correspond to $\text{Na}_2\text{Mn}_5\text{O}_{10}$ (marked as ▼, JCPDS Card No. 27-0749) [26], and the intensity of the peaks in the XRD patterns increases with the rise of hydrothermal reaction temperature. As reported previously, $\text{Na}_2\text{Mn}_5\text{O}_{10}$ has a microporous structure (0.46 nm × 0.69 nm) arising from the edge sharing of 2 × 3 $[\text{MnO}_6]$ octahedral chains to form a one-dimensional tunnel structure [27]. The XRD patterns of catalysts prepared with different Na:Mn molar ratios were also measured, with the results shown in Fig. 2B. It is clear from Fig. 2Ba and b that the $\text{Na}_{0.25}\text{Mn}_y\text{O}_8\text{-}120$ and $\text{Na}_{0.5}\text{Mn}_y\text{O}_8\text{-}120$ catalysts with Na:Mn ratios

(lower than 0.5) are composed of $\text{Na}_2\text{Mn}_5\text{O}_{10}$ and Mn_2O_3 crystalline phases. For the $\text{Na}_{0.75}\text{Mn}_y\text{O}_8\text{-}120$ and $\text{Na}_{1.5}\text{Mn}_y\text{O}_8\text{-}120$ catalysts (Fig. 2Bc and d), the Mn_2O_3 crystal phase cannot be observed, and the diffraction peaks of $\text{Na}_2\text{Mn}_5\text{O}_{10}$ gradually grew in intensity with a further increase in NaNO_3 content. Furthermore, as the Na:Mn molar ratio further increases to 2, the diffraction peaks with high intensities ($2\theta = 15.8^\circ, 32.2^\circ, 39.8^\circ, 44.6^\circ$) were observed for the $\text{Na}_2\text{Mn}_y\text{O}_8\text{-}120$ catalyst, which can be assigned as the characteristic peaks of $\text{Na}_2\text{Mn}_3\text{O}_7$ (marked as △, JCPDS Card No. 78-0193) [28], and the intensities of the diffraction peaks of $\text{Na}_2\text{Mn}_5\text{O}_{10}$ crystalline phase decrease to a great extent. For clarity, the crystal phase compositions and crystal sizes of each catalyst are summarized in Table 1. Table 1 shows that the hydrothermal reaction temperature and Na:Mn molar ratio have important effects on the crystal size of the catalyst. With an increase in the hydrothermal reaction temperature, the crystal size of the catalysts increased gradually, while the crystal size of all the catalysts was in the range of 5.8–30.8 nm with an increase in the Na:Mn molar ratio.

Visible Raman spectroscopy at an excitation wavelength of 532 nm was used to further study the phase structure of the $\text{Na}_x\text{Mn}_y\text{O}_8$ catalysts, and the results are shown in Figs. 2C and 2D. As presented in Fig. 2Ca-c, the bands of the $\text{Na}_0\text{Mn}_y\text{O}_8\text{-}T$ catalysts at 311.6, 642.4, and 697.9 cm^{-1} are observed to be in agreement with the literature reference values of bixbyite Mn_2O_3 [29]. These bands can be assigned to the out-of-plane bending modes, asymmetric stretching of bridging oxygen species ($\text{Mn}-\text{O}-\text{Mn}$), and symmetric stretching of Mn_2O_3 groups, respectively [30,31]. Compared with the $\text{Na}_0\text{Mn}_y\text{O}_8\text{-}T$ catalysts, the $\text{Na}_1\text{Mn}_y\text{O}_8\text{-}T$ catalysts (Fig. 2 Cd-f) exhibit a significantly increased number of Raman bands. For the $\text{Na}_1\text{Mn}_y\text{O}_8\text{-}T$ catalysts, the bands in the range of 550–750 cm^{-1} can be assigned to the stretching modes of the Mn–O bonds in MnO_6 octahedra, and the weaker intensity bands in the ranges of 200–450 cm^{-1} and 450–550 cm^{-1} may correspond to skeletal vibrations and deformation modes of the Mn–O–Mn chains in the octahedral lattice, respectively. These spectra are very similar to those of the romanechite manganese oxides reported in the literature [32], which further proves that the $\text{Na}_1\text{Mn}_y\text{O}_8\text{-}T$ catalysts feature a characteristic $\text{Na}_2\text{Mn}_5\text{O}_{10}$ crystal phase. Fig. 2D displays the Raman spectra of catalysts prepared with different Na:Mn molar ratios. As shown in Fig. 2 Da, the Raman bands of $\text{Na}_{0.25}\text{Mn}_y\text{O}_8\text{-}120$ can be observed at wavelengths of 290.2, 381.8, 510.2, 580.5, 622.3, 642.4, and 720.5 cm^{-1} , which are almost the same as those of $\text{Na}_1\text{Mn}_y\text{O}_8\text{-}T$. It is worth noting that there are new Raman peaks at 311.6 cm^{-1} (dotted box) and 659.7 cm^{-1} (Fig. 2 Da and 2Db), which, in combination with the XRD results, may be interpreted to be due to the presence of Mn_2O_3 in the samples [33,34]. As the Na:Mn ratio increases to 0.75, the Raman band intensities at 311.6 cm^{-1} and 659.7 cm^{-1} significantly decrease, which corresponds to the disappearance of the Mn_2O_3 crystal phase. In addition, the band located at 720.5 cm^{-1} cannot be observed when the Na:Mn ratio is 2. According

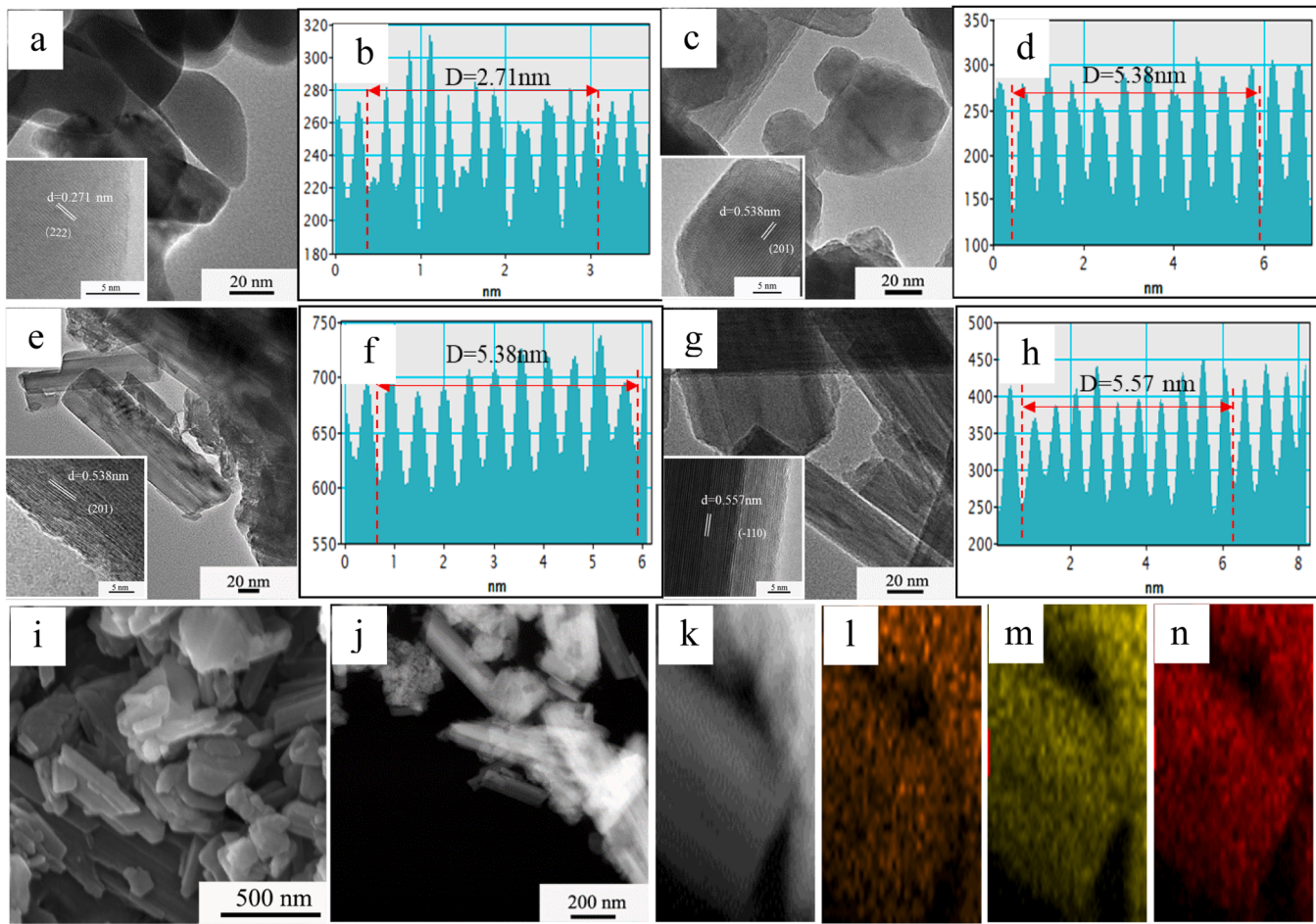


Fig. 3. TEM and HRTEM images of as-prepared catalysts (a, b: $\text{Na}_0\text{Mn}_y\text{O}_8\text{-}120$; c, d: $\text{Na}_{0.25}\text{Mn}_y\text{O}_8\text{-}120$; e, f: $\text{Na}_1\text{Mn}_y\text{O}_8\text{-}120$; g, h: $\text{Na}_2\text{Mn}_y\text{O}_8\text{-}120$), SEM (i), HAADF-STEM (j, k), EDS elemental mappings images (l: Na; m: Mn; n: O) of $\text{Na}_1\text{Mn}_y\text{O}_8\text{-}120$ catalyst.

to literature reports [32], the peak positions of romanechite manganese oxide are similar to those of layered manganese oxide, except for the Raman band at 720.5 cm^{-1} , which further verifies that the $\text{Na}_2\text{Mn}_y\text{O}_8\text{-}120$ catalyst features a $\text{Na}_2\text{Mn}_3\text{O}_7$ phase.

3.2. Morphological and texture properties

As is well known, soot catalytic combustion is a heterogeneous catalytic reaction that occurs at the three-phase (gas ($\text{O}_2/\text{NO}/\text{NO}_2$)-solid (catalyst)-solid (soot)) contact interface. The morphologies of soot oxidation catalysts have a significant effect on the contact efficiency between the soot and the catalysts. The morphologies of the $\text{Na}_x\text{Mn}_y\text{O}_8$ catalysts were observed using SEM and TEM techniques, and the results are shown in Fig. 3, S1, and S2. Fig. S1a-c show that the prepared $\text{Na}_0\text{Mn}_y\text{O}_8\text{-T}$ catalysts exhibit an irregular blunt-shaped micro-cluster nanostructure formed by the coalescence of smaller crystals. There are apparent differences in the size of the nanostructures and the surface of particles at different hydrothermal reaction temperatures, which may be related to the anisotropic growth of the crystals. In contrast with the $\text{Na}_0\text{Mn}_y\text{O}_8\text{-T}$ catalysts, it was clear that the morphologies of the $\text{Na}_1\text{Mn}_y\text{O}_8\text{-T}$ catalysts changed considerably when NaNO_3 was added under the same hydrothermal conditions, and they mainly transformed from irregular small particles to large and thick rod-shaped structures (Fig. 3i and S1d, e). Meanwhile, these morphologies were maintained at different hydrothermal reaction temperatures, even with other Na:Mn molar ratios, as shown in Fig. 3i and Fig. S2. Notably, the $\text{Na}_2\text{Mn}_y\text{O}_8\text{-}120$ catalyst with a Na:Mn ratio of 2 exhibits an elongated rod-like structure (Fig. S2e). Generally, there is no obvious alteration in the microstructure

of catalysts prepared with different Na:Mn molar ratios.

Fig. 3a-h shows the TEM and high-resolution TEM (HRTEM) images of the $\text{Na}_0\text{Mn}_y\text{O}_8\text{-}120$, $\text{Na}_{0.25}\text{Mn}_y\text{O}_8\text{-}120$, $\text{Na}_1\text{Mn}_y\text{O}_8\text{-}120$, and $\text{Na}_2\text{Mn}_y\text{O}_8\text{-}120$ catalysts. As shown in Fig. 3a, the $\text{Na}_0\text{Mn}_y\text{O}_8\text{-}120$ catalyst possesses a morphology of accumulated nanoparticles in various shapes. The introduction of Na ions changes the morphologies of the $\text{Na}_{0.25}\text{Mn}_y\text{O}_8\text{-}120$, $\text{Na}_1\text{Mn}_y\text{O}_8\text{-}120$, and $\text{Na}_2\text{Mn}_y\text{O}_8\text{-}120$ catalysts to be rod-like (Fig. 3c, e, g), which is consistent with the SEM images. Meanwhile, the HRTEM images suggest that the as-prepared catalysts are highly crystalline, as evidenced by the clear lattice fringes. As shown in the inset of Fig. 3a, the lattice fringe spacing of $\text{Na}_0\text{Mn}_y\text{O}_8\text{-}120$ is 0.271 nm, determined by calculating the average of 10 lattice fringes (Fig. 3b), which can be assigned to the (222) planes of Mn_2O_3 with a face-centered cubic structure. For the $\text{Na}_{0.25}\text{Mn}_y\text{O}_8\text{-}120$ and $\text{Na}_1\text{Mn}_y\text{O}_8\text{-}120$ catalysts (Fig. 3c-f), the interplanar spacing of 0.538 nm, determined by calculating the average of 10 lattice fringes for two vertical crystal planes, is observed, corresponding to the (201) plane of the $\text{Na}_2\text{Mn}_5\text{O}_{10}$ phase. The lattice spacing of the $\text{Na}_2\text{Mn}_y\text{O}_8\text{-}120$ catalyst is 0.557 nm, corresponding to the (-110) crystal plane of $\text{Na}_2\text{Mn}_3\text{O}_7$, which is consistent with the XRD results (Fig. 2B). The high-angle annular dark-field scanning TEM (HAADF-STEM) images and energy-dispersive X-ray spectroscopy (EDS) elemental mappings of the $\text{Na}_1\text{Mn}_y\text{O}_8\text{-}120$ catalyst are shown in Fig. 3j-n. It can be seen from Fig. 3j that the bright part of the image corresponds to the nanorods of the $\text{Na}_1\text{Mn}_y\text{O}_8\text{-}120$ catalyst. Fig. 3k (a section of Fig. 3j) was selected for EDS scanning to obtain the EDS elemental mappings of Na, Mn, and O. Fig. 3l-n further show that all the elements are evenly distributed on the $\text{Na}_1\text{Mn}_y\text{O}_8\text{-}120$ nanorods, indicating that the catalyst is a complex

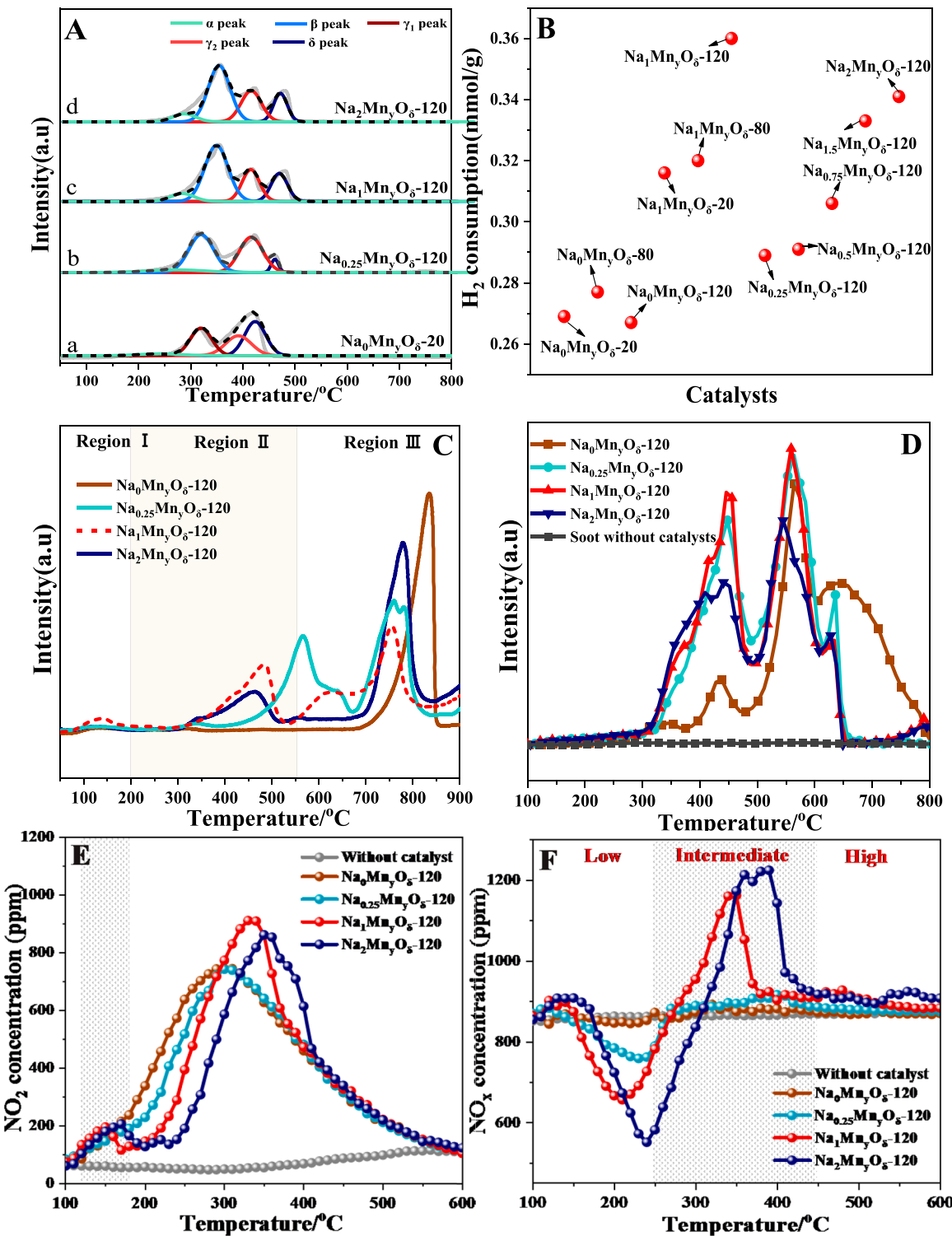


Fig. 4. H_2 -TPR (A) and Hydrogen consumption amount (B), O_2 -TPD (C), Soot-TPR (D) and NO_x -TPO (E, F) profiles of as-prepared $Na_xMn_yO_8$ catalysts.

composition of Na, Mn, and O elements. There are noticeable significant differences in the densities of each element, with densities ranging from high to low for Na (orange), Mn (yellow), and O (red), which are consistent with a $Na_2Mn_5O_{10}$ crystal phase.

The nitrogen (N_2) adsorption–desorption results and Brunauer–Emmett–Teller (BET) surface areas of the as-prepared $Na_xMn_yO_8$ catalysts are displayed in Fig. S3 and Table 1. According to the classification of hysteresis loops and adsorption isotherms by IUPAC, the $Na_xMn_yO_8$ catalysts exhibit type IV adsorption isotherm curves and a H3

hysteresis loop in the range of $P/P_0 = 0.9$ –1.0. Combined with SEM and TEM images (Fig. 3, S1 and S2), the rapid increase of nitrogen adsorption quantity at this pressure is related to the pore structure generated by the accumulation of catalyst particles. Table 1 shows that the textural properties of $Na_xMn_yO_8$ catalysts are influenced by the preparation conditions. According to the results in Table 1, it can be easily observed that the BET surface areas of the $Na_0Mn_yO_8$ -T catalysts decrease slightly with an increase in the reaction temperature, while those of the $Na_1Mn_yO_8$ -T catalysts slightly increase. Furthermore, the BET surface

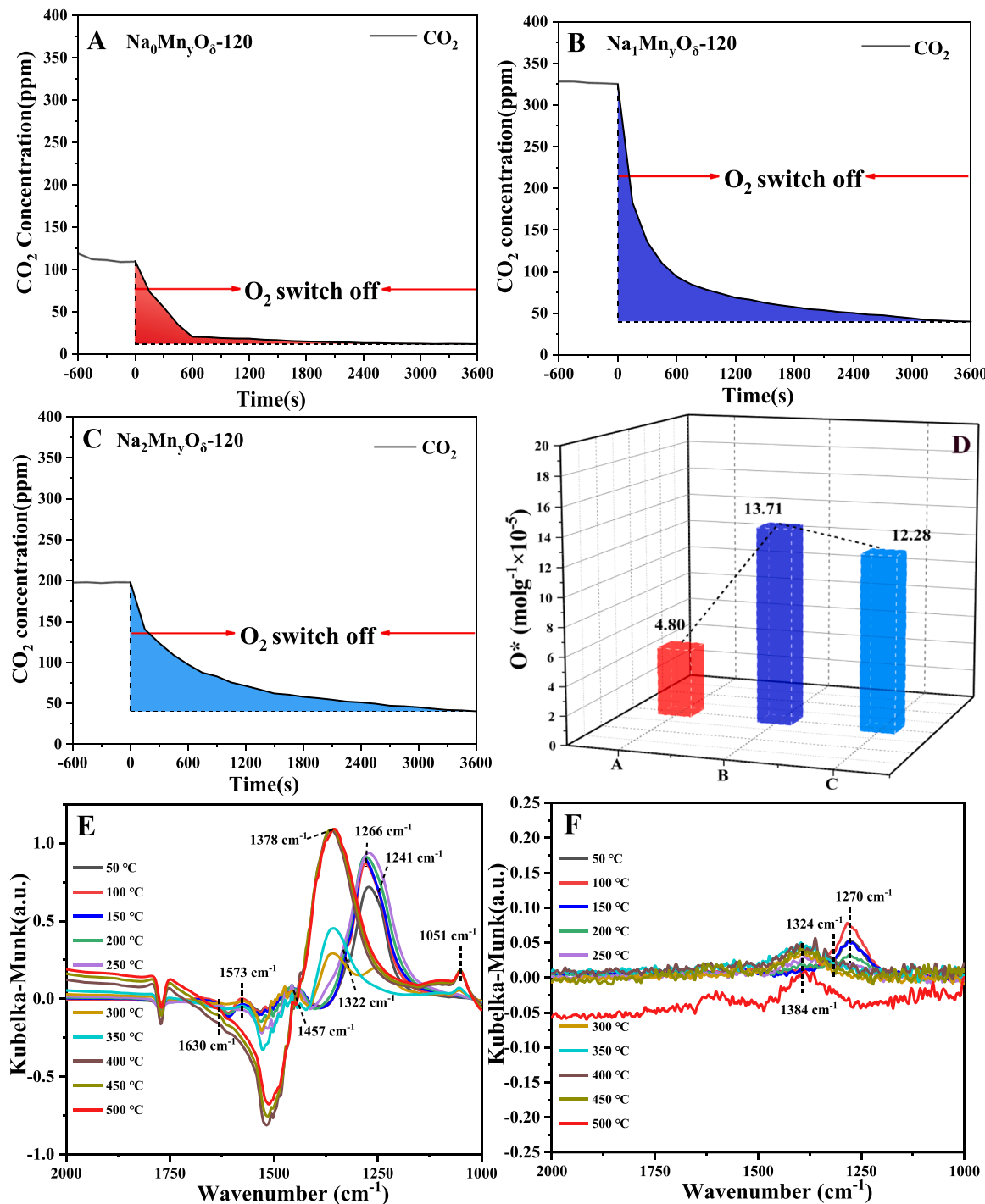


Fig. 8. The CO₂ concentrations profiles (A, B, C) as a function of time at 270 °C before and after moving of O₂ in the reactant atmosphere, active oxygen amount (D) of catalysts during isothermal soot oxidation over the $\text{Na}_0\text{Mn}_y\text{O}_\delta$ -120 (a), $\text{Na}_1\text{Mn}_y\text{O}_\delta$ -120 (b) and $\text{Na}_2\text{Mn}_y\text{O}_\delta$ -120 (c) catalysts and in situ DRIFT spectra of NO_x adsorption on $\text{Na}_1\text{Mn}_y\text{O}_\delta$ -120 catalyst (E) and $\text{Na}_1\text{Mn}_y\text{O}_\delta$ -120 with soot (F) as a function of temperature under a gas mixture of 0.2 vol% NO/ 10 vol% O₂/Ar.

areas of the catalysts prepared with different Na:Mn ratios increase to a certain extent, from 5.8 m²/g to 13.1 m²/g, in line with the increase in the Na:Mn ratios. This is primarily because morphological alteration weakens the aggregation of particles (Fig. S2), hence increasing the specific surface area. In other words, the different preparation conditions may result in the differences in the morphologies and texture properties of the $\text{Na}_x\text{Mn}_y\text{O}_\delta$ catalysts.

3.3. Redox properties

The reducibility of catalysts is vital for their performance in heterogeneous deep oxidation reactions. Therefore, H₂-TPR measurements were conducted to evaluate the reducibility of the catalysts, and the results are shown in Fig. 4A, Fig. S4, and Table S2. The peaks of the H₂-TPR curves of the $\text{Na}_x\text{Mn}_y\text{O}_\delta$ catalysts are divided into four peaks, labeled as α , β , γ (γ_1 , γ_2), and δ reduction peaks. The α reduction peaks at 241 °C–288 °C correspond to the consumption of structural oxygen near the catalyst surface. As is well known, the reduction of MnO_x is usually a

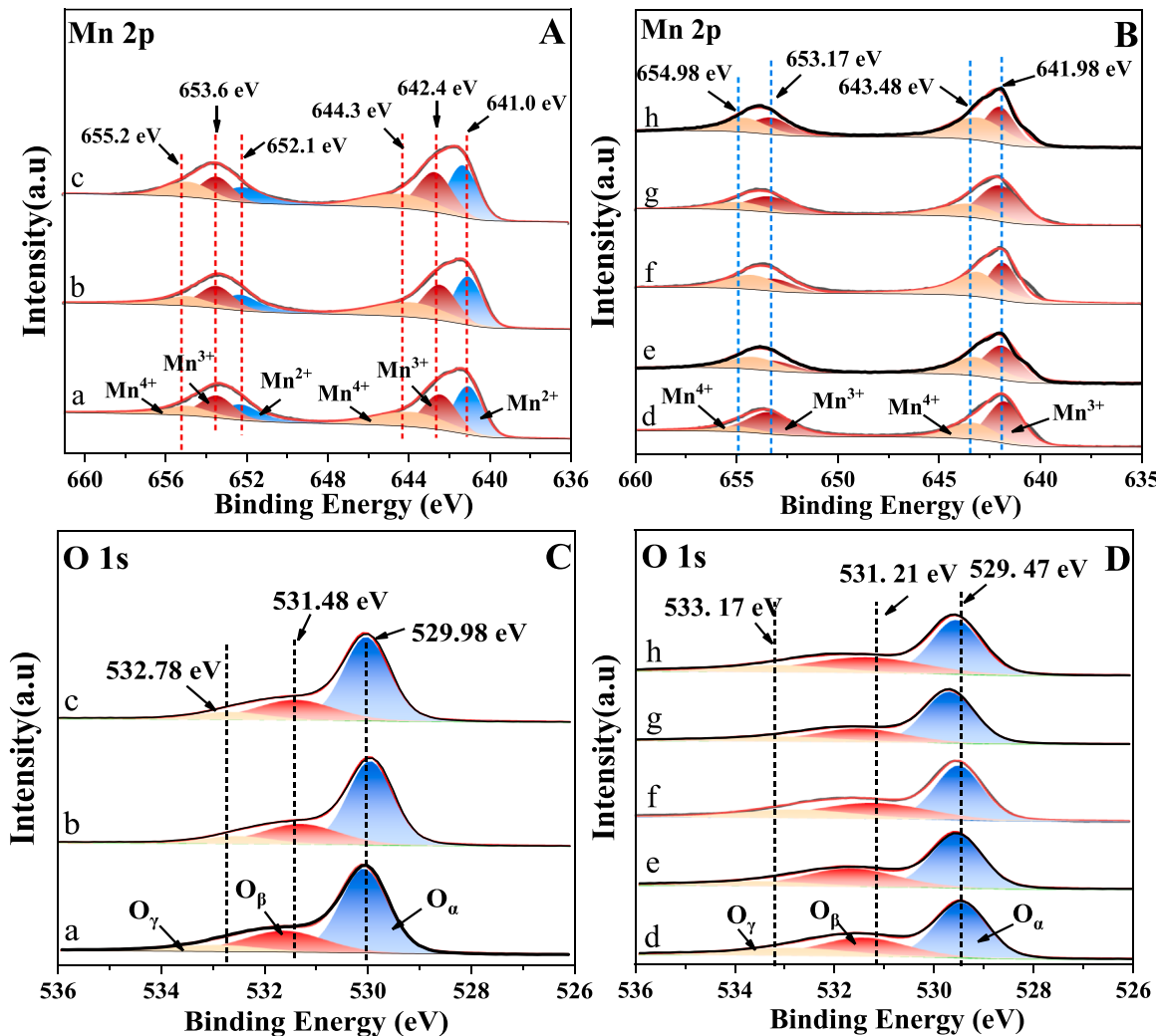


Fig. 5. The Mn2p (A, B), O1s (C, D) XPS spectra of as-prepared catalysts (a: $\text{Na}_0\text{Mn}_y\text{O}_\delta$ -20; b: $\text{Na}_0\text{Mn}_y\text{O}_\delta$ -80; c: $\text{Na}_0\text{Mn}_y\text{O}_\delta$ -120; d: $\text{Na}_1\text{Mn}_y\text{O}_\delta$ -20; e: $\text{Na}_1\text{Mn}_y\text{O}_\delta$ -80; f: $\text{Na}_1\text{Mn}_y\text{O}_\delta$ -120; g: $\text{Na}_{0.25}\text{Mn}_y\text{O}_\delta$ -120; h: $\text{Na}_2\text{Mn}_y\text{O}_\delta$ -120).

Table 2

Surface compositions and oxidation states of O and Mn species over as-prepared catalysts derived from XPS analyses.

Catalyst	O species (%)				Mn species (%)			(AOS) ^c
	O_α	O_β	O_γ	R ^a	Mn^{4+}	Mn^{3+}	Mn^{2+}	
$\text{Na}_0\text{Mn}_y\text{O}_\delta$ -20	64.37	25.66	9.97	0.398	29.24	32.42	38.34	0.413
$\text{Na}_0\text{Mn}_y\text{O}_\delta$ -80	65.62	24.84	9.53	0.378	28.75	31.73	39.53	0.404
$\text{Na}_0\text{Mn}_y\text{O}_\delta$ -120	64.67	26.47	8.86	0.409	29.21	32.48	38.31	0.413
$\text{Na}_1\text{Mn}_y\text{O}_\delta$ -20	56.56	31.94	11.51	0.564	46.06	53.94	-	0.854
$\text{Na}_1\text{Mn}_y\text{O}_\delta$ -80	55.91	33.56	10.54	0.600	50.14	49.86	-	1.005
$\text{Na}_1\text{Mn}_y\text{O}_\delta$ -120	53.75	32.76	13.50	0.609	60.07	39.93	-	1.504
$\text{Na}_{0.25}\text{Mn}_y\text{O}_\delta$ -120	60.00	27.35	12.65	0.455	40.87	59.13	-	0.691
$\text{Na}_2\text{Mn}_y\text{O}_\delta$ -120	54.21	31.29	14.50	0.577	54.51	45.49	-	1.198

^a The O species ratio of the $\text{O}_\beta/\text{O}_\alpha$

^b The Mn species ratio of the $\text{Mn}^{4+}/(\text{Mn}^{3+} + \text{Mn}^{2+})$

^c AOS stands for average oxidation state of Mn element

successive reduction process in the form of $\text{MnO}_x \rightarrow \text{Mn}_2\text{O}_3 \rightarrow \text{Mn}_3\text{O}_4 \rightarrow \text{MnO}$ [35,36]. For $\text{Na}_0\text{Mn}_y\text{O}_\delta$ -T catalysts, the γ_1 reduction peaks at 314 °C–343 °C and γ_2 reduction peaks at 385 °C–406 °C can be assigned to surface and bulk $\text{Mn}_2\text{O}_3 \rightarrow \text{Mn}_3\text{O}_4$ reduction processes, respectively. Meanwhile, the δ peaks at 411 °C–441 °C can be assigned to the $\text{Mn}_3\text{O}_4 \rightarrow \text{MnO}$ reduction process. For the $\text{Na}_{x>0}\text{Mn}_y\text{O}_\delta$ -T catalysts, the β , γ_2 , and δ reduction peaks can be attributed to $\text{MnO}_x \rightarrow \text{Mn}_2\text{O}_3$, $\text{Mn}_2\text{O}_3 \rightarrow \text{Mn}_3\text{O}_4$, and $\text{Mn}_3\text{O}_4 \rightarrow \text{MnO}$ reduction processes, respectively. Generally speaking, the reducibility of catalysts is mainly reflected by

the reduction temperature and hydrogen consumption. The lower the reduction peak temperature and the more hydrogen consumed, the greater the reducibility of the catalysts. As can be seen from Fig. 4A, Fig. S4, and Table S2, there is no significant difference in the temperatures of the main reduction peaks between the $\text{Na}_0\text{Mn}_y\text{O}_\delta$ -T and $\text{Na}_{x>0}\text{Mn}_y\text{O}_\delta$ -T catalysts. It is worth noting that the hydrogen consumption significantly increases when Na is introduced into the catalysts, as shown in Fig. 4B. Among the $\text{Na}_{x>0}\text{Mn}_y\text{O}_\delta$ -T catalysts, the total H_2 consumption amount per gram of catalysts follows the order

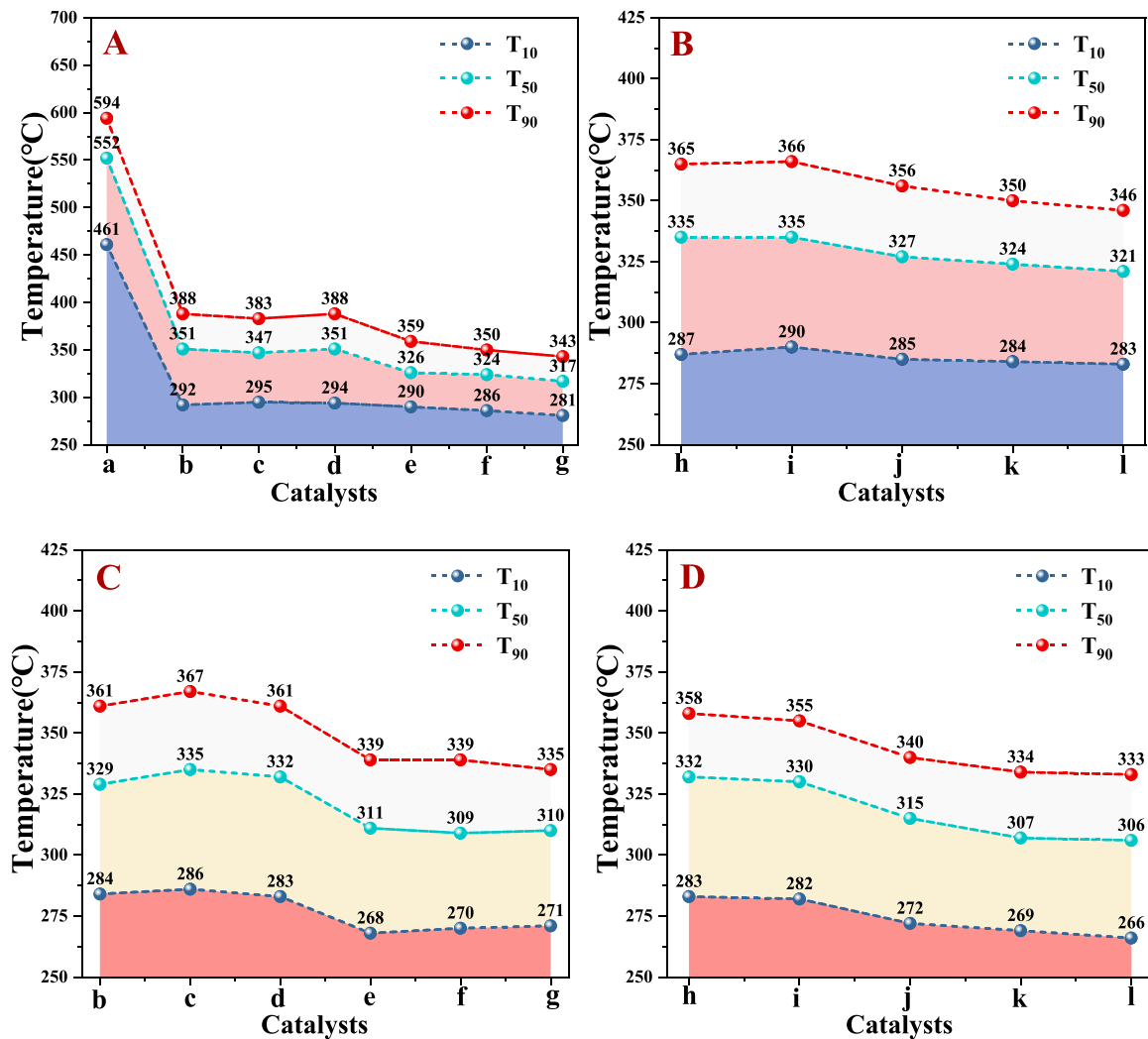


Fig. 6. Catalytic activities of as-prepared $\text{Na}_x\text{Mn}_y\text{O}_\delta$ catalysts for soot combustion ((A, B) 2000 ppm NO, 10% O_2 , and Ar balance; (C, D) 2000 ppm NO, 10% O_2 , 10% H_2O and Ar balance; a: Pure soot; b: $\text{Na}_0\text{Mn}_y\text{O}_\delta$ -20; c: $\text{Na}_0\text{Mn}_y\text{O}_\delta$ -80; d: $\text{Na}_0\text{Mn}_y\text{O}_\delta$ -120; e: $\text{Na}_1\text{Mn}_y\text{O}_\delta$ -20; f: $\text{Na}_1\text{Mn}_y\text{O}_\delta$ -80; g: $\text{Na}_1\text{Mn}_y\text{O}_\delta$ -120; h: $\text{Na}_{0.25}\text{Mn}_y\text{O}_\delta$ -120; i: $\text{Na}_{0.5}\text{Mn}_y\text{O}_\delta$ -120; j: $\text{Na}_{0.75}\text{Mn}_y\text{O}_\delta$ -120; k: $\text{Na}_{1.5}\text{Mn}_y\text{O}_\delta$ -120; l: $\text{Na}_2\text{Mn}_y\text{O}_\delta$ -120).

of $\text{Na}_1\text{Mn}_y\text{O}_\delta$ -120 > $\text{Na}_2\text{Mn}_y\text{O}_\delta$ -120 > $\text{Na}_{1.5}\text{Mn}_y\text{O}_\delta$ -120 > $\text{Na}_1\text{Mn}_y\text{O}_\delta$ -80 > $\text{Na}_1\text{Mn}_y\text{O}_\delta$ -20 > $\text{Na}_{0.75}\text{Mn}_y\text{O}_\delta$ -120 > $\text{Na}_{0.5}\text{Mn}_y\text{O}_\delta$ -120 > $\text{Na}_0\text{Mn}_y\text{O}_\delta$ -80 > $\text{Na}_0\text{Mn}_y\text{O}_\delta$ -20 > $\text{Na}_0\text{Mn}_y\text{O}_\delta$ -120. This indicates that $\text{Na}_{x>0}\text{Mn}_y\text{O}_\delta$ -T catalysts exhibit better reducibility than $\text{Na}_0\text{Mn}_y\text{O}_\delta$ -T catalysts, and the activities of soot oxidation catalysts are greatly dependent on their reducibility.

To explore the role of oxygen species in soot combustion, O_2 -TPD measurements were conducted over the as-prepared $\text{Na}_x\text{Mn}_y\text{O}_\delta$ catalysts, with the results shown in Fig. 4C and Fig. S5. The O_2 -TPD curves of the catalysts are divided into three regions based on the temperature range. Region I (50 °C–200 °C) corresponds to oxygen species physically or surface adsorbed on a weak adsorption center, Region II (200 °C–550 °C) can be assigned to chemisorbed oxygen species that strongly interact with cations or defects on the catalyst surface, and Region III (>550 °C) is attributed to the desorption of near-surface/sub-surface lattice oxygen and bulk lattice oxygen species. According to literature reports, the reactive oxygen species (ROS) in Region II play a significant role in improving catalytic activity [37,38]. The results suggest that the desorption peaks of the oxygen species in Region II cannot be clearly observed for the $\text{Na}_0\text{Mn}_y\text{O}_\delta$ -T catalysts. However, for the $\text{Na}_1\text{Mn}_y\text{O}_\delta$ -120 catalysts containing Na ions, the intensities of the desorption peaks in Region II increase gradually with the increase of hydrothermal reaction temperature. In addition, the desorption peaks of

the $\text{Na}_1\text{Mn}_y\text{O}_\delta$ -80, $\text{Na}_{0.25}\text{Mn}_y\text{O}_\delta$ -120 and $\text{Na}_2\text{Mn}_y\text{O}_\delta$ -120 catalysts can also be observed in the same region, but for the $\text{Na}_{0.25}\text{Mn}_y\text{O}_\delta$ -120 catalyst, the desorption peak of the chemisorbed oxygen species shows a noticeable shift toward a higher temperature. Among all the catalysts, the $\text{Na}_1\text{Mn}_y\text{O}_\delta$ -120 catalyst exhibits a lower desorption temperature and a higher amount of desorbed amount of reactive oxygen species. This indicates that it may have strong ability to adsorb and activate gaseous oxygen, resulting in the $\text{Na}_1\text{Mn}_y\text{O}_\delta$ -120 catalyst exhibiting high catalytic activity for soot oxidation.

To further investigate the intrinsic oxidation capacity of the $\text{Na}_0\text{Mn}_y\text{O}_\delta$ -120, $\text{Na}_{0.25}\text{Mn}_y\text{O}_\delta$ -120, $\text{Na}_1\text{Mn}_y\text{O}_\delta$ -120, and $\text{Na}_2\text{Mn}_y\text{O}_\delta$ -120 catalysts, soot-TPR measurements were performed under a high-purity argon (Ar) atmosphere, and the profiles are shown in Fig. 4D. By comparing the soot-TPR curve without catalysts, it can be obtained that the generated CO_2 originates from the oxidation of soot particles by oxygen species on the surface or bulk phase of the prepared catalysts. According to the soot-TPR results, the CO_2 profiles can be divided into two temperature regions, among which the region I (300–500 °C) can be attributed to surface oxygen species (O_2 , O_2^-) and region II (500 °C–800 °C) corresponds to lattice oxygen (O_2^-), respectively. For the $\text{Na}_x\text{Mn}_y\text{O}_\delta$ catalysts, the temperature ranges of CO_2 generated by soot oxidation are almost the same, but its concentration varies significantly in the presence of the different catalysts. This phenomenon is

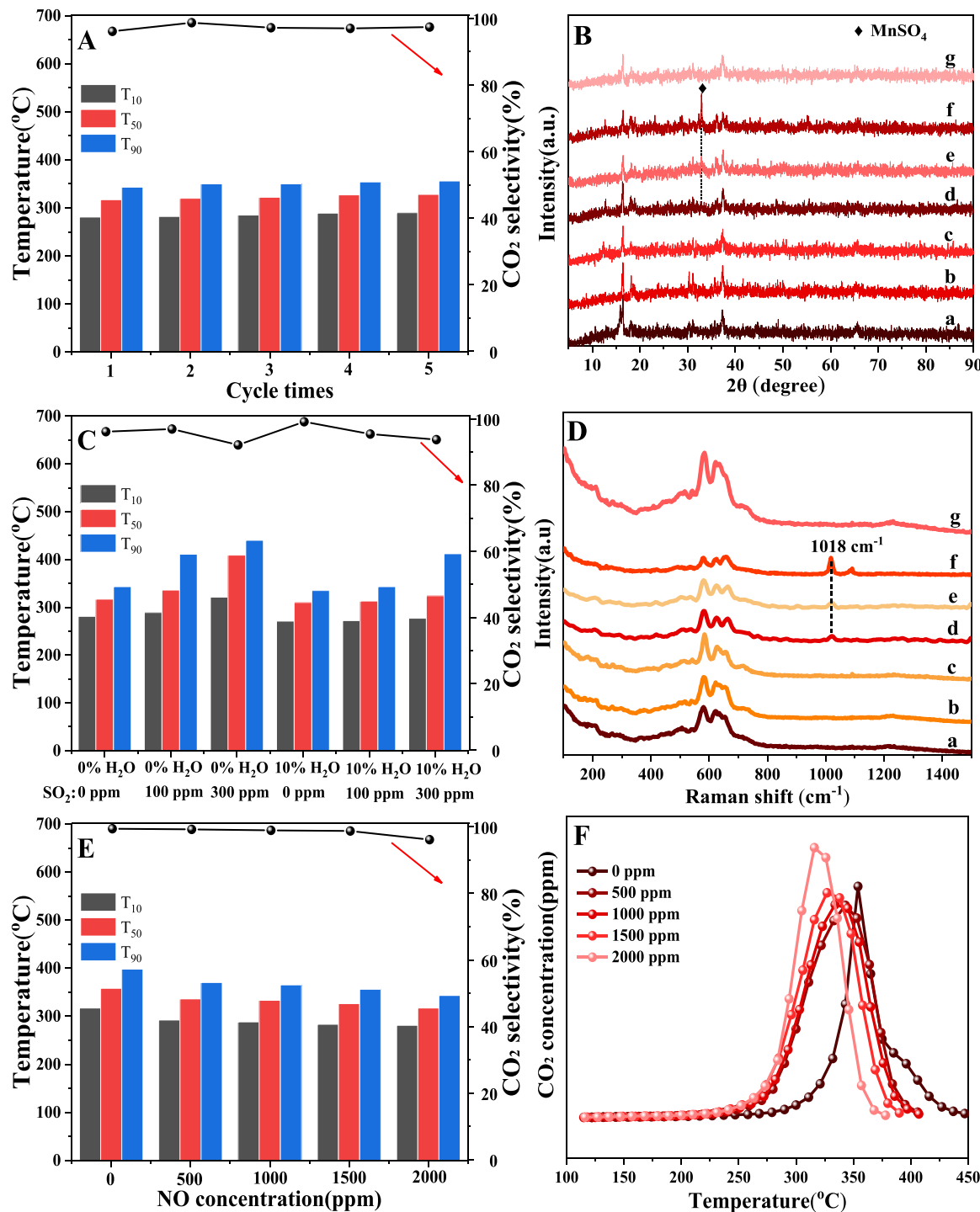


Fig. 7. The stability (A), water and sulfur resistance (C), XRD patterns (B), and Raman spectra (D) of the $\text{Na}_1\text{Mn}_1\text{O}_8\text{-120}$ catalyst under different reaction atmospheres (a: Fresh catalyst; b: 10% H_2O +0 ppm SO_2 ; c: 10% H_2O +100 ppm SO_2 ; d: 0% H_2O +100 ppm SO_2 ; e: 10% H_2O +300 ppm SO_2 ; f: 0% H_2O +300 ppm SO_2 ; g: used catalyst after 5th cycle reaction), catalytic performance (E) and CO_2 concentration profiles(F) under different NO concentrations.

mainly influenced by the desorption temperature and amount of surface and bulk oxygen species of the $\text{Na}_x\text{Mn}_y\text{O}_\delta$ catalysts. As can be seen from Fig. 4D, compared with the $\text{Na}_0\text{Mn}_1\text{O}_8\text{-120}$ catalysts, a higher desorption amount of surface-adsorbed oxygen can be observed for the $\text{Na}_1\text{Mn}_1\text{O}_8\text{-120}$ and $\text{Na}_2\text{Mn}_1\text{O}_8\text{-120}$ catalysts, which is consistent with the $\text{O}_2\text{-TPD}$ results. These results further confirm that the tunnel-structured $\text{Na}_2\text{Mn}_5\text{O}_{10}$ phase is more conducive to the adsorption and activation of oxygen to generate ROS than the layered $\text{Na}_2\text{Mn}_3\text{O}_7$ and Mn_2O_3 phases, thereby improving the activity of the soot oxidation

catalysts.

The great majority of NO_x species, as is well known, mainly exist in the form of NO in diesel exhaust. Thereby, the ability of NO oxidation to NO_2 over $\text{Na}_x\text{Mn}_y\text{O}_\delta$ catalysts is significant for enhancing the catalytic performance of soot combustion. Figs. 4E, 4F, and Fig. S6 display the NO-TPO profiles over the $\text{Na}_0\text{Mn}_1\text{O}_8\text{-120}$, $\text{Na}_1\text{Mn}_1\text{O}_8\text{-120}$, $\text{Na}_{0.25}\text{Mn}_1\text{O}_8\text{-120}$, and $\text{Na}_2\text{Mn}_1\text{O}_8\text{-120}$ catalysts. By way of comparison, the NO-TPO measurements were also conducted in the absence of a catalyst. The results in Figs. 4E, 4F, and Fig. S6 show that the NO, NO_2 , and NO_x

Table 3

Reaction rate, active oxygen (O^*) amount and density, TOF values for isothermal soot oxidation reaction over $Na_0Mn_yO_6$ -120, $Na_1Mn_yO_6$ -120 and $Na_2Mn_yO_6$ -120 catalysts.

Catalysts	Temperature/°C	v ($mols^{-1}g^{-1} \times 10^{-7}$) ^a	v* ($mols^{-1}m^{-2} \times 10^{-9}$) ^b	O^* ($molg^{-1} \times 10^{-5}$) ^c	O^* density (nm ⁻²) ^d	TOF (s ⁻¹ × 10 ⁻³) ^e
$Na_0Mn_yO_6$ -120	270	0.61	4.65	4.80	2.20	1.27
$Na_1Mn_yO_6$ -120	270	1.83	19.89	13.71	8.97	1.33
$Na_2Mn_yO_6$ -120	270	1.11	9.49	12.28	6.32	0.90

^a Reaction rate.

^b The specific reaction rate normalized by unit BET surface area.

^c The amount of active oxygen

^d The density of active oxygen

^e The ratio of the reaction rate to active site amount.

concentrations do not change significantly in the absence of catalysts within the tested temperature range. On the contrary, the concentrations of NO_x species appear to show evident variations in the presence of the $Na_xMn_yO_6$ catalysts. Among them, it can be clearly observed that the concentration of NO_2 first increases and then decreases (Fig. 4E), while the concentration of NO shows the opposite trend with an increase in temperature (Fig. S6). This indicates that NO is mainly converted to NO_2 with the effect of catalysts during the soot oxidation process rather than being directly oxidized by O_2 at elevated temperatures. Obviously, the maximum NO_2 concentration of the $Na_1Mn_yO_6$ -120 catalyst is higher than those of the other three catalysts, implying that the catalyst exhibits better NO-to- NO_2 oxidation ability. Moreover, the difference is that $Na_1Mn_yO_6$ -120 and $Na_2Mn_yO_6$ -120 catalysts exhibit a trend of first increasing and then decreasing in the low-temperature range of 100 °C–200 °C, followed by a slow increase before 300 °C. Based on the in-situ DRIFT characterization results in Fig. 8E, it can be concluded that the consumption of NO_2 is caused by the formation of nitrate or nitrite under the action of oxygen species on the $Na_1Mn_yO_6$ -120 and $Na_2Mn_yO_6$ -120 catalyst surface. This further demonstrates the adsorption and activation of NO species by alkali metals in the above catalysts. In the total NO_x profiles, the $Na_{x>0}Mn_yO_6$ catalysts decrease in different degrees at low temperature temperatures (100 °C–250 °C), first increasing and then decreasing at intermediate temperature (250 °C–450 °C), and then stabilize at high temperature (450 °C–600 °C). These phenomena can all be attributed to the rapid chemical adsorption or reaction of NO on the catalyst surface at the low-temperature stage and the desorption of adsorbed or reacted NO_x during the intermediate-temperature stage. It is generally known that NO_2 is a stronger oxidizer than O_2 for soot combustion [39]. Therefore, it can be concluded that the $Na_1Mn_yO_6$ -120 catalyst exhibits good catalytic activity because of its strong NO oxidation ability, NO_x storage, and desorption capacity.

3.4. Chemical states

To investigate the element distribution and oxidation valence state on the catalyst surface, the Na, Mn, and O elements of $Na_xMn_yO_6$ catalysts were characterized by XPS, and the results are shown in Fig. 5, Fig. S7, and Table 2. The survey XPS spectra in Fig. S7A and S7B indicate that Mn and O elements are found in the $Na_0Mn_yO_6$ -T catalysts, while the $Na_{x>0}Mn_yO_6$ -T catalysts also contain Na element, which were well consistent with the composition of the catalysts. Fig. S7C displays the Na 1 s XPS spectra of the $Na_{x>0}Mn_yO_6$ -T catalysts. It can be clearly observed that the Na 1 s XPS spectrum has a single peak at a binding energy of around 1071 eV. However, the peak intensity of the $Na_{0.25}Mn_yO_6$ -120 catalyst is significantly lower than that of the other catalysts. This phenomenon can be attributed to the relatively lower content of Na in the catalyst, which is consistent with the XRD results.

Figs. 5A and 5B display the Mn 2p XPS spectra of the as-prepared catalysts, which show two similar Mn 2p_{3/2} and Mn 2p_{1/2} peaks with binding energies at 641.68–641.98 eV and 653.47–653.76 eV, respectively. However, due to the overlapping peaks of the Mn^{n+} species, it is

difficult to reliably distinguish the valence states and quantify these Mn species only from the Mn 2p spectra. To further verify the valence states of the Mn species, the Mn 3 s spectra are shown in Fig. S8. Generally, the split width of the Mn 3 s peak (ΔE) is sensitive to the oxidation valence state of the Mn species on the catalyst surface. As shown in Fig. S8, the ΔE values of the $Na_0Mn_yO_6$ -T catalysts range from 5.7 eV to 5.9 eV, and the ΔE values of the $Na_{x>0}Mn_yO_6$ catalysts are 4.62–4.86 eV. The average oxidation state (AOS) values of Mn element were calculated according to the equation: $AOS = 8.956 - 1.126 \times \Delta E$ [40]; that is, a lower ΔE Mn 3 s peak value corresponds to a higher oxidation state. Therefore, the valence states and Mn species content on the $Na_xMn_yO_6$ catalyst surface can be further analyzed based on the AOS values.

The Mn 2p spectra of the $Na_0Mn_yO_6$ -T catalysts were fitted to six characteristic peaks corresponding to Mn ions with +2, +3, and +4 valence states on the catalyst surface. The Mn 2p_{3/2} peaks centered at around 641.0, 642.4, and 644.3 eV can be assigned to Mn^{2+} , Mn^{3+} , and Mn^{4+} components, while the corresponding coupled Mn 2p_{1/2} peaks are split at 655.2, 653.6, and 652.1 eV, respectively [41]. The appearance of Mn^{4+} can be generally attributed to the partial oxidation of Mn^{3+} on the surface of the Mn_2O_3 phase [42]. For $Na_{x>0}Mn_yO_6$ -T catalysts, the Mn 2p_{3/2} spectra can be deconvoluted into two peaks at ~641.98 eV and ~643.48 eV, corresponding to Mn^{3+} and Mn^{4+} species, and the peaks at ~653.17 eV and ~654.98 eV correspond to Mn^{3+} and Mn^{4+} in the Mn 2p_{1/2} spectra, respectively [43,44]. In contrast with the $Na_0Mn_yO_6$ -T catalysts, the Mn element on the $Na_{x>0}Mn_yO_6$ -T catalysts surface exists in the form of Mn^{3+} and Mn^{4+} . As is well known, Mn species with a higher oxidation state are preferable for oxidation reactions [45,46]. Therefore, the surface $Mn^{4+}/(Mn^{3+} + Mn^{2+})$ relative ratios (R_1) were calculated from the integrated area of fitting peaks in the deconvolution spectra, and the results are summarized in Table 2, which indicate the surface enrichment degree of the Mn^{4+} component. The R_1 values are in the order of $Na_1Mn_yO_6$ -120 (150.41%) > $Na_2Mn_yO_6$ -120 (119.81%) > $Na_1Mn_yO_6$ -80 (100.54%) > $Na_1Mn_yO_6$ -20 (85.38%) > $Na_{0.25}Mn_yO_6$ -120 (69.13%) > $Na_0Mn_yO_6$ -20 (41.32%) ≈ $Na_0Mn_yO_6$ -80 (41.26%) ≈ $Na_0Mn_yO_6$ -120 (40.35%). This suggests that the Mn^{4+} content on the catalyst surface significantly increases due to the introduction of Na ions, and the $Na_1Mn_yO_6$ -120 catalyst exhibits the highest Mn^{4+} content of 60.07%. In addition, the AOS values of the $Na_xMn_yO_6$ catalysts are listed in Table 2, where it can be seen that the order of AOS values is consistent with the order of the molar ratio of $Mn^{4+}/(Mn^{3+} + Mn^{2+})$, as supported by the Mn 2p results.

Figs. 5C and 5D show the O 1 s spectra of the $Na_xMn_yO_6$ catalysts, which can be divided into three types of oxygen species by peak fitting, assigned to lattice oxygen species (O_α : O^{2-}) at ca. 529.47–529.98 eV, surface-adsorbed oxygen species (O_β : O_2^- or O_2^{2-}) at ca. 531.21–531.73 eV, and physically-adsorbed oxygen species (O_γ : O_2) at 532.78–533.17 eV, respectively. According to relevant literature, surface-adsorbed oxygen (O_β) plays a vital role during the oxidation process of soot particles. Therefore, the ratio of O_β oxygen species to O_α oxygen species (R^b) can be estimated from the relative amounts of oxygen species calculated, as listed in Table 2. It can be concluded that the adsorbed oxygen content on the surface of the $Na_0Mn_yO_6$ -T catalysts is

basically the same, while that on the $\text{Na}_1\text{Mn}_y\text{O}_8\text{-T}$ catalyst surface substantially increases after the introduction of Na ions. This is mainly due to the O_2 molecule adsorbing on the $\text{Na}_1\text{Mn}_y\text{O}_8$ surface with an oxygen defect and O_2 also adsorbing at two adjacent Mn^{4+} ions in a bidentate manner when NO oxidation occurs on manganese oxides and then dissociating into two active O^* , attaining the lowest reaction potential barrier [47]. Therefore, the increase in the surface Mn^{4+} species is one of the reasons that contributes to the enrichment of surface reactive oxygen species, which is further supported by the O 1 s XPS results. Among the catalysts, the $\text{Na}_1\text{Mn}_y\text{O}_8\text{-120}$ has a higher abundance of O_β species ($R = 0.609$), in agreement with the $\text{O}_2\text{-TPD}$ results, which is also the main reason for its excellent catalytic performance in soot combustion.

3.5. Catalytic performance for soot combustion

3.5.1. Catalytic activities of the $\text{Na}_x\text{Mn}_y\text{O}_8$ catalysts

The catalytic activities of the as-prepared $\text{Na}_x\text{Mn}_y\text{O}_8$ catalysts were investigated by temperature-programmed oxidation (TPO) reaction under O_2 (10 vol%) and NO (2000 ppm) conditions balanced with Ar, and the results are shown in Figs. 6A, 6B, and Table S3. Meanwhile, soot combustion in the absence of a catalyst was also conducted under the same reaction conditions, in which the T_{10} , T_{50} , and T_{90} values are 461 °C, 552 °C, and 594 °C, respectively. Compared with the combustion temperature of pure soot particles, all the $\text{Na}_x\text{Mn}_y\text{O}_8$ catalysts significantly reduce the soot combustion temperature, which is lower than the exhaust temperature (<450 °C). As depicted in Fig. 6A, the effect of the hydrothermal reaction temperature on the catalytic activities of the $\text{Na}_0\text{Mn}_y\text{O}_8\text{-T}$ catalysts is not obvious in the absence of Na ions. However, for the $\text{Na}_{x>0}\text{Mn}_y\text{O}_8$ catalysts, the catalytic activities increased significantly with the increase in the reaction temperature in the presence of Na ions, especially in the medium and late stages of the soot oxidation reaction (see the corresponding T_{50} and T_{90} values). It can be observed that the catalytic activities of the catalysts exhibit a volcanic distribution as the Na:Mn molar ratio increases. Among them, the $\text{Na}_1\text{Mn}_y\text{O}_8\text{-120}$ catalyst exhibits the highest catalytic activity, with T_{10} , T_{50} , and T_{90} values of 281 °C, 317 °C, and 343 °C, respectively, and a high CO_2 selectivity of 96.1% (Fig. 6B and Table S3). It is worth mentioning that the catalytic activity of the $\text{Na}_1\text{Mn}_y\text{O}_8\text{-120}$ catalyst is similar to or even higher than the performance of noble-metal-based catalysts in the medium (T_{50}) and high (T_{90}) temperature ranges. Furthermore, the catalytic activities of $\text{Na}_1\text{Mn}_y\text{O}_8\text{-120}$ catalyst are also investigated at various heating rates, with the light-off curves shown in Fig. S9. The results reveal that the light-off curves shift towards high-temperature direction with the increase of heating rates. As the heating rate increases from 2 °C/min to 10 °C/min, the burnout temperature (T_{90}) values rise from 343 °C to 431 °C, which is still lower than the temperature range of diesel engine exhaust outlet, suggesting that $\text{Na}_1\text{Mn}_y\text{O}_8\text{-120}$ catalyst has high catalytic activity for soot oxidation. The outstanding catalytic performance of the $\text{Na}_1\text{Mn}_y\text{O}_8\text{-120}$ catalysts may be ascribed to improved redox capacity, more surface reactive oxygen species, and abundant surface Mn^{4+} ions, which can be satisfactorily explained by the measurements based on $\text{H}_2\text{-TPR}$, $\text{O}_2\text{-TPD}$, and XPS analysis. Additionally, to investigate the influence of H_2O in the diesel engine exhaust on the catalytic performance of the $\text{Na}_x\text{Mn}_y\text{O}_8$ catalysts, soot-TPO experiments were conducted under O_2 (10 vol%), NO (2000 ppm), and H_2O (10%) conditions balanced with Ar, and the results are shown in Figs. 6C, 6D, and Table S4. The results illustrate that the H_2O vapor is beneficial to catalytic soot combustion, in agreement with previous reports [48,49]. The main reasons for this phenomenon are as follows. On the one hand, the wettability of water vapor increases the contact efficiency between the active site of the catalysts and soot particles; on the other hand, it may be due to the formation of protonated species (such as nitric or nitrous acids) or the reduction of activation energy of the catalytic soot combustion reaction. From Figs. 6C, 6D, and Table S4, it can be seen that the T_{10} , T_{50} , and T_{90} values of the $\text{Na}_1\text{Mn}_y\text{O}_8\text{-T}$ catalysts are significantly lower than those of the

$\text{Na}_0\text{Mn}_y\text{O}_8\text{-T}$ catalysts, which is consistent with the trend shown in the absence of water vapor. The difference is that the catalytic activities of the $\text{Na}_{x>0}\text{Mn}_y\text{O}_8\text{-120}$ catalysts show an increasing trend in line with an increase in the Na:Mn molar ratios. This is slightly different from the trend in the activity of the $\text{Na}_{x>0}\text{Mn}_y\text{O}_8\text{-120}$ catalysts in the presence of 10% H_2O , which may be caused by the strong ability of alkali metals to adsorb nitrogen oxides, thus accelerating the cyclic reaction between protonated species and NO_x species.

3.5.2. Stability, water and sulfur resistance, and activity at different NO concentrations of the $\text{Na}_1\text{Mn}_y\text{O}_8\text{-120}$ catalysts

Stability is an essential factor by which to measure the performance of catalysts in practical applications. As a consequence, the stability of the $\text{Na}_1\text{Mn}_y\text{O}_8\text{-120}$ catalyst was examined via five catalytic soot-TPO cycles under an atmosphere containing 10% O_2 , 2000 ppm NO, and Ar balance, as shown in Fig. 7A and Table S5. The stability test results demonstrate that the $\text{Na}_1\text{Mn}_y\text{O}_8\text{-120}$ catalyst possesses excellent stability after five soot combustion reaction cycles, as can be inferred from slight variations in the T_{10} , T_{50} , and T_{90} values of 285 °C ± 5 °C, 322 °C ± 5 °C, and 350 °C ± 6 °C, respectively. Meanwhile, the CO_2 selectivity remains stable, exceeding 96% after five reaction cycles. In addition, to further verify its stability, after the stability tests the $\text{Na}_1\text{Mn}_y\text{O}_8\text{-120}$ catalyst was characterized using XRD and Raman spectroscopy, the results of which are displayed in Fig. 7B_g and 7D_g. It was found that the XRD patterns and Raman spectra of the used catalyst are basically the same as those of the fresh catalyst, revealing that the structure of the $\text{Na}_1\text{Mn}_y\text{O}_8\text{-120}$ catalyst remains stable after the catalytic oxidation of soot particles.

As is well known, the study of the effect of SO_2 in diesel engine exhaust on the catalytic activity of a catalyst is of great significance for soot combustion. Therefore, to evaluate the sulfur resistance of the $\text{Na}_1\text{Mn}_y\text{O}_8\text{-120}$ catalyst, its performance was measured under different SO_2 concentrations (100 ppm and 300 ppm SO_2), with the results shown in Fig. 7C and Table S6. According to the data, there is a certain degree of decline in the catalytic activity of the $\text{Na}_1\text{Mn}_y\text{O}_8\text{-120}$ catalyst in the presence of 100 ppm SO_2 , with an increase in its T_{10} , T_{50} , and T_{90} values to 289 °C, 336 °C, and 411 °C, respectively. As the concentration of SO_2 increases to 300 ppm, the catalyst activity further decreases, and the CO_2 selectivity decreases to 92.1%. To further explore the sulfur tolerance of the $\text{Na}_1\text{Mn}_y\text{O}_8\text{-120}$ catalyst in practical applications, the catalytic performance of the $\text{Na}_1\text{Mn}_y\text{O}_8\text{-120}$ catalyst was also investigated under a reaction atmosphere containing sulfur and water vapor. The results, displayed in Fig. 7C, indicate that the water vapor in the reaction atmosphere contributes to the catalytic combustion reaction of soot particles, which also occurs in the presence of SO_2 . Under the concentration of SO_2 (100 ppm) and water (10%), the $\text{Na}_1\text{Mn}_y\text{O}_8\text{-120}$ catalyst exhibits high catalytic performance, and its T_{10} , T_{50} , and T_{90} values are similar to those in the absence of SO_2 and water. Under a reaction atmosphere of 300 ppm SO_2 and 10% H_2O , the activity of the catalyst decreases to a certain extent, especially during the high-temperature stage (T_{90}). Moreover, with an increase in SO_2 concentration, the CO_2 selectivity of the catalyst decreases slightly to 93.7%. This phenomenon reveals that SO_2 in the reaction atmosphere has a negative effect on the catalytic performance of the $\text{Na}_1\text{Mn}_y\text{O}_8\text{-120}$ catalyst. To further investigate the main reason for the differences in the catalytic performance of the catalyst under different reaction conditions, the used samples were characterized by XRD and Raman spectroscopy. From the XRD results (Fig. 7B), it can be seen that a new diffraction peak ($2\theta = 33.1^\circ$, marked as ♦) is observed at SO_2 concentrations of 100 ppm and 300 ppm in the absence of water vapor [50,51], the intensity of which increases gradually with an increase in SO_2 concentration. However, in the presence of water vapor, the intensity of the above diffraction peak decreases, and it is only observable at high SO_2 concentrations. Fig. 7D shows the Raman spectra of the used $\text{Na}_1\text{Mn}_y\text{O}_8\text{-120}$ catalyst after water and sulfur resistance measurements. As can be seen in Fig. 7Dd-f, there is a new Raman peak located at 1018 cm^{-1} upon the introduction of SO_2 to the

reaction atmosphere, which can be attributed to the vibration of S–O bonds [52], and its strength increases along with the SO₂ concentration. These results indicate that the reduction in catalytic activity is mainly due to the reaction of manganese components with SO₂ to form manganese sulfate (MnSO₄) species. Moreover, the presence of H₂O weakens the intensity of the new peaks related to MnSO₄. Therefore, it can be further inferred that the MnSO₄ formed on the catalyst surface affects the contact between the active component and soot particles in the absence of H₂O vapor. However, the water molecules react with SO₂ to form sulfuric or sulfite acid in the presence of H₂O, which may improve the contact between soot particles and the catalyst by wetting the surface of the catalyst, thus facilitating the soot oxidation reaction. In general, the introduction of H₂O vapor reduces or moderates the formation of sulfate species on the catalyst surface, which is why the atmosphere containing both H₂O vapor and SO₂ is more active than that containing SO₂ alone.

As mentioned above, the NO reactant, as an important intermediate, has a significant effect on soot oxidation. To explore the relationship between NO concentration and catalytic activity, the activity evaluation

was carried out under different NO concentrations over the Na₁Mn₅O₆-120 catalyst. As shown in Fig. 7E and Table S7, the catalytic activity of the Na₁Mn₅O₆-120 catalyst is the lowest when NO is absent from the reaction atmosphere, and its T_{10} , T_{50} , and T_{90} values are 317 °C, 358 °C, and 398 °C, respectively. When NO is introduced into the reaction system (500 ppm), the catalytic performance of the Na₁Mn₅O₆-120 catalyst improves greatly, with T_{10} , T_{50} , and T_{90} values of 292 °C, 336 °C, and 370 °C, respectively. With an increase in the NO concentration, the catalytic activity (especially at high temperature (T_{90})) is further enhanced, and the CO₂ selectivity of the catalyst is greater than 96%. Fig. 7F shows the CO₂ concentration curves of the catalytic oxidation of soot under different NO concentrations. As illustrated in these profiles, the corresponding CO₂ concentration curves shift toward a lower temperature direction as the NO concentration increases, and the temperature is the lowest (317 °C) at an NO concentration of 2000 ppm. This phenomenon is consistent with the NO-TPO results, demonstrating that the oxidation of NO to NO₂ is a crucial step during the soot oxidation process.

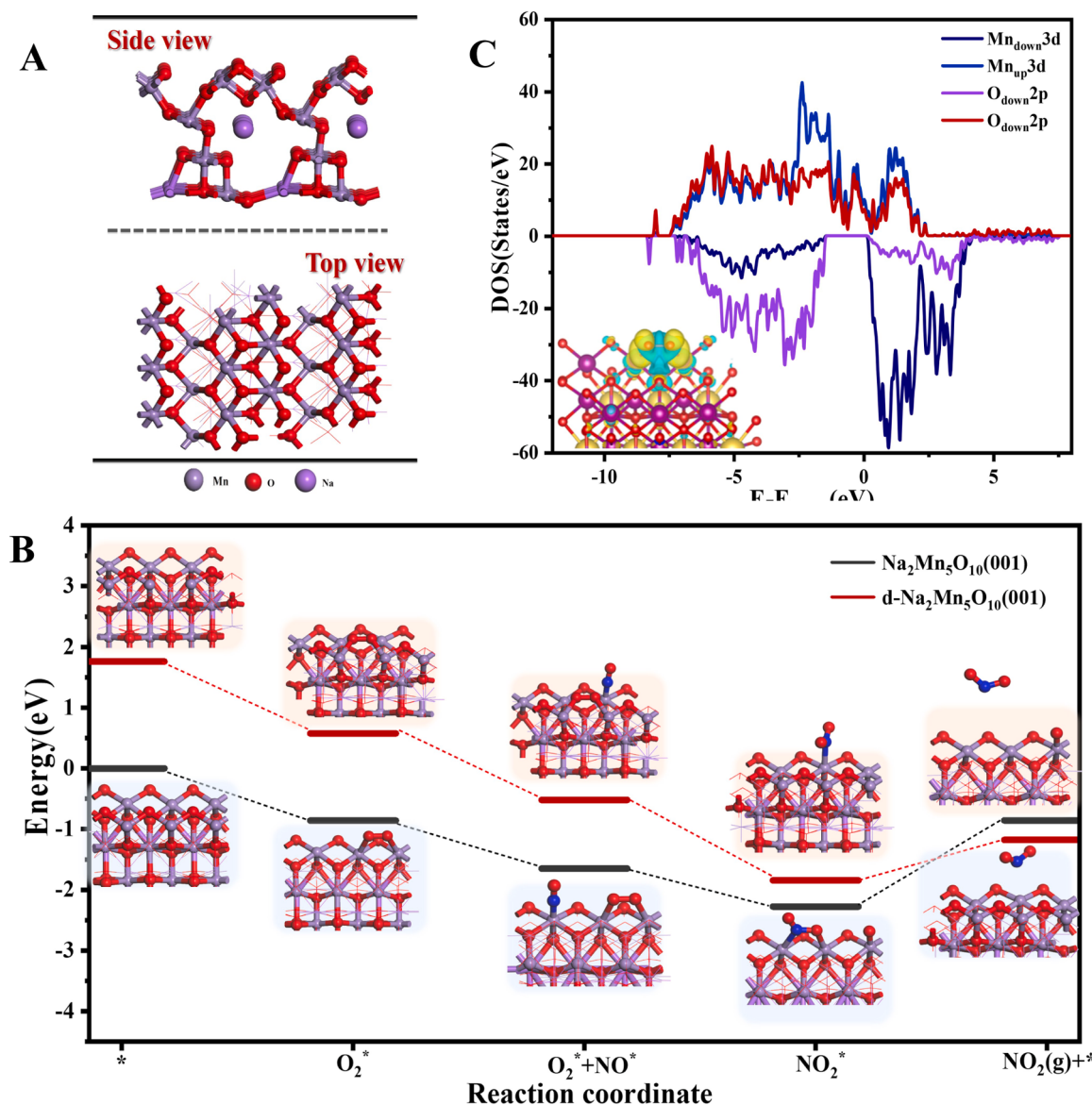


Fig. 9. (A) Side view and top view of Na₂Mn₅O₁₀ (001), (B) reaction pathway of NO catalytic oxidation to generate NO₂ on Na₂Mn₅O₁₀ (001) surface and oxygen-defective surface d-Na₂Mn₅O₁₀ (001), and (C) projected partial density of states (PDOS) of Na₂Mn₅O₁₀ (001) with adsorbed oxygen. The inset is electron density difference upon the interaction between the active O₂ and Na₂Mn₅O₁₀ (001). Accumulation region in yellow and depletion regions in blue.

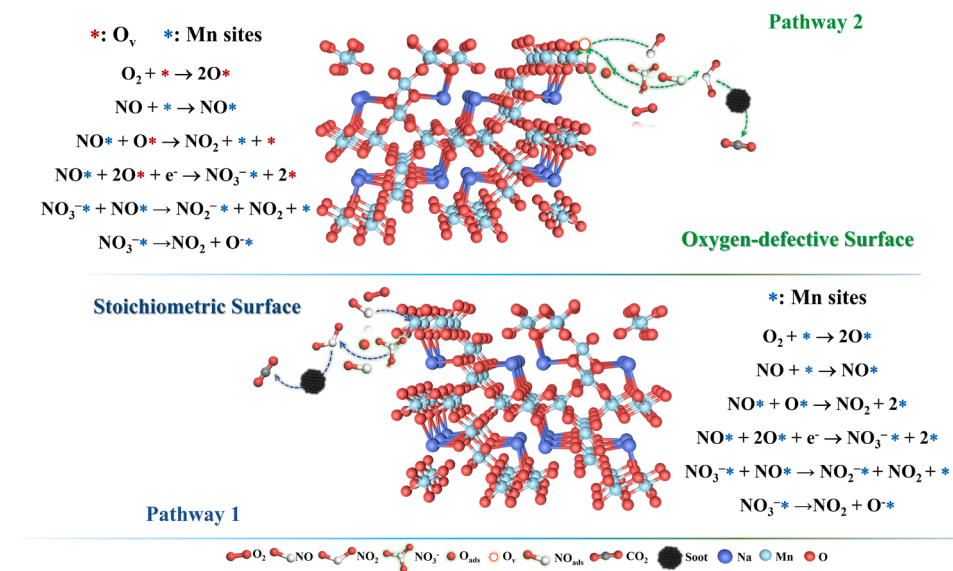


Fig. 10. Schematic illustration of catalysts with $Na_2Mn_5O_{10}$ phase in soot catalytic oxidation.

3.5.3. Isothermal kinetic study and in-situ DRIFTS of the NO_x adsorption of the $Na_xMn_yO_\delta$ catalysts

Isothermal kinetic reactions can be utilized for determining the reaction rate, number of active sites, and the turnover frequency (TOF) values of $Na_xMn_yO_\delta$ catalysts for soot combustion [53]. Fig. 8A–C show the CO_2 concentration curves of the $Na_0Mn_yO_8$ -120, $Na_1Mn_yO_8$ -120, and $Na_2Mn_yO_8$ -120 catalysts at 270 °C before and after removal of O_2 from the reactant atmosphere. The quantified values of the reaction rate, amount of active oxygen, and the TOF values over the above catalysts for soot oxidation are also summarized in Table 3. The data in Table 3 show that the reaction rate of the isothermal reaction over the $Na_1Mn_yO_8$ -120 catalyst is significantly higher than those of the $Na_0Mn_yO_8$ -120 and $Na_2Mn_yO_8$ -120 catalysts. Moreover, to eliminate the influence of the specific surface area, the specific reaction rates (v^*) of the $Na_xMn_yO_\delta$ catalysts normalized by the unit BET surface area are also listed in Table 3. The $Na_1Mn_yO_8$ -120 catalyst exhibits the highest specific reaction rate, 4.27 and 2.09 times those of the $Na_0Mn_yO_8$ -120 and $Na_2Mn_yO_8$ -120 catalysts, which is consistent with its apparent catalytic activity. Generally, gaseous O_2 can be adsorbed on the active sites of catalysts during isothermal experiments and is then activated to active oxygen species (O^\ast) to oxidize nearby soot particles into CO_2 . Therefore, the active sites of the catalysts can be quantified by integrating the CO_2 generation rate that decreases with time after oxygen interruption in the isothermal soot combustion reaction [54]. Fig. 8D shows that the quantities of active oxygen species (O^\ast) are 4.80×10^{-5} mol·g⁻¹ ($Na_0Mn_yO_8$ -120), 13.71×10^{-5} mol·g⁻¹ ($Na_1Mn_yO_8$ -120), and 12.28×10^{-5} mol·g⁻¹ ($Na_2Mn_yO_8$ -120), respectively. Among them, $Na_1Mn_yO_8$ -120 has the highest amount of active oxygen species and the highest O^\ast density, which further indicates the superior catalytic activity of the catalyst. Moreover, the TOF values of catalysts were also calculated according to the ratio of the reaction rates and the quantity of O^\ast , as listed in Table 3. The TOF values decrease in the order of $Na_1Mn_yO_8$ -120 (1.33×10^{-3} s⁻¹) > $Na_0Mn_yO_8$ -120 (1.27×10^{-3} s⁻¹) > $Na_2Mn_yO_8$ -120 (0.90×10^{-3} s⁻¹). For the $Na_xMn_yO_\delta$ catalysts, the consistency between the TOF and activity sequence of the catalysts further indicates that the $Na_1Mn_yO_8$ -120 catalyst exhibits relatively higher intrinsic activity compared to the other catalysts. However, the TOF of the $Na_2Mn_yO_8$ -120 catalyst is contrary to its activity sequence, implying that the introduction of Na ions enhances the NO adsorption and oxidation capability of the catalyst under actual reaction atmospheres. In this work, the quantity of active oxygen species (O^\ast) appears to be the fundamental reason for the catalyst showing effectively

improved combustion activity of soot particles.

To gain insight into the surface-adsorbed NO_x species on the $Na_1Mn_yO_8$ -120 catalyst, in-situ DRIFTS as a function of temperature were acquired under an atmosphere of 2000 ppm NO, 10% O_2 , and Ar balance, as shown in Figs. 8E and 8F. The in-situ DRIFTS spectra were recorded at intervals of 50 °C from 50 °C to 500 °C, and the spectra were obtained after the catalyst was exposed to an NO atmosphere for 2 min at each temperature. For the $Na_1Mn_yO_8$ -120 catalyst (Fig. 8E), the vibration bands in the DRIFT spectra can be attributed to chelated nitro compounds (1241 cm^{-1}), monodentate nitrates (1266 cm^{-1}), nitro compounds (1322 cm^{-1}), monodentate nitrite (1457 cm^{-1}), bidentate nitrates (1573 cm^{-1}), and weakly adsorbed NO_2 (1630 cm^{-1}) in the low-temperature region (50–250 °C), respectively [55–59]. Upon an increase in the temperature to 300 °C, a new band is observed at 1378 cm^{-1} , which can be attributed to ionic nitrates, and its intensity increases gradually with an increase in temperature. Moreover, to explore the intermediates on the catalyst surface during the soot combustion process, in-situ DRIFTS measurements were conducted on a mixture of $Na_1Mn_yO_8$ -120 catalyst and soot particles under the same reaction atmosphere. The results in Fig. 8F show that the NO_x species adsorbed on the soot–catalyst mixture are similar to those adsorbed in the absence of soot particles. Evidently, NO_x -derived adsorbents, such as monodentate nitrate (1270 cm^{-1}) and nitro compounds (1324 cm^{-1}), decompose or convert to ionic nitrate NO_3^- (1384 cm^{-1}) with an increase in temperature. The intermediate species NO_3^- further reacts with NO to generate NO_2 as follows: $NO_3^- + NO \rightarrow NO_2 + NO_2$.⁴⁹ The results of in-situ DRIFTS measurements further indicate that the nitrate/nitrite adsorbed on the surface of the catalyst plays a major role in the soot combustion process, thus affecting the catalytic activity of $Na_1Mn_yO_8$ -120.

3.5.4. DFT results and reaction mechanism of the $Na_2Mn_5O_{10}$ catalysts for soot combustion

Density functional theory (DFT) calculations were performed to study the reaction mechanism of NO oxidation on the $Na_2Mn_5O_{10}$ catalysts. The $Na_2Mn_5O_{10}$ catalysts have a unique 2×3 rectangular tunnel structure with calculated lattice constants of $a = 13.47\text{ \AA}$, $b = 2.89\text{ \AA}$, and $c = 9.80\text{ \AA}$, respectively. A stoichiometric $Na_2Mn_5O_{10}$ (001) surface and oxygen-defective d- $Na_2Mn_5O_{10}$ (001) surface were constructed to study the reaction mechanism as the (001) facet exhibits a low surface energy and abundant exposed metal sites. Fig. 9 A shows the top and side views of the $Na_2Mn_5O_{10}$ (001) surface, which features a five-

coordinated Mn, three-coordinated oxygen (O_{III}), and two-coordinated oxygen (O_{II}) atoms. The formation energies of the oxygen vacancies are 1.76 eV for O_{II} and 3.00 eV for O_{III} atoms; thus, the O_{II} vacancy is more easily generated. Fig. 9B shows the energy profiles for the oxidation of NO to NO_2 on the $Na_2Mn_5O_{10}$ (001) and d- $Na_2Mn_5O_{10}$ (001) surfaces. On $Na_2Mn_5O_{10}$ (001), O_2 is adsorbed on Mn sites with an adsorption energy of -0.86 eV, with a change in the bond length of O_2 from 1.24 Å to 1.30 Å, and the overlapped peaks of the Mn 3d states with the O 2p states imply strong orbital interactions between Mn and O atoms, as shown in the projected partial density of states (PDOS) in Fig. 9C. Charge-density difference analysis also reveals obvious electron transfer and strong chemical bonding. These results demonstrate that O_2 can be adsorbed and activated effectively. The desorption energy of NO_2 on active sites is 1.42 eV, and NO oxidation occurs via the L-H mechanism. While, on d- $Na_2Mn_5O_{10}$ (001), O_2 prefer to adsorbed on oxygen vacancies with an adsorption energy of -1.36 eV, accompanied by a change in the O_2 bond length from 1.24 Å to 1.32 Å, with a change in the active site Mn site to an oxygen vacancy. The desorption energy of NO_2 is 0.67 eV, which indicates that oxygen vacancies promote the activation of O_2 and the desorption process of NO_2 , thus improving the activity of the catalyst.

Based on the above DFT calculation and various characterization results, reaction mechanisms were proposed for soot combustion over the catalysts with $Na_2Mn_5O_{10}$ phase in the NO and O_2 reaction system. As depicted in Fig. 10, two reaction pathways can be observed during the catalytic combustion of soot particles. The first reaction pathway is as follows: Mn sites serve as the main active sites in the process of adsorbate activation on the stoichiometric surface of $Na_2Mn_5O_{10}$ catalysts. Gaseous O_2 interacts with Mn sites on the catalyst surface to form reactive oxygen species (O_2^-/O^-), and gaseous NO is also adsorbed on Mn sites to form the adsorbed NO. Then, the reactive oxygen species react with adsorbed NO to generate adsorbed NO_2 . The desorbed NO_2 serves as oxygen carrier to transfer surface oxygen to soot particles and form surface oxidation complexes (SOC) (carbon and oxygen compounds), thus transforming the gas (NO/O_2)-solid (catalyst)-solid (soot) reaction into a gas (NO/O_2)-gas (NO_2)-solid (soot) reaction, greatly improving the contact efficiency between the catalysts and soot particles. Finally, the SOC decompose into CO and CO_2 [60]. In addition, the adsorbed NO also reacts with reactive oxygen species on the surface of the catalyst to form nitrate or nitrite species, as supported by in-situ DRIFT results (Figs. 8E and 8F). With increasing of temperature, these intermediate species decompose from the surface of the catalysts to form NO_2 , which then reacts with soot particles to form CO_2 . The above results indicate that the Langmuir-Hinshelwood reaction pathway is the main reaction mechanism over the $Na_2Mn_5O_{10}$ catalysts. The second reaction pathway is proposed based on the oxygen-defective surface. Mn sites and oxygen vacancies are two active sites, which are involved in this reaction pathway. O_2 prefers to adsorb on the oxygen vacancies of the catalyst surface. The reactive oxygen activated by the oxygen vacancies and Mn ions, will react with adsorbed NO to generate NO_2 on the Mn sites and further oxidize the soot particles. In addition, Wang et al. [61] studied the adsorption of gas with the dynamic diameter of less than 0.4 nm on the OMS-2 catalyst and found that gas molecules with the kinetic diameter of less than 0.33 nm would enter the 2×2 tunnel structure of OMS-2. The result indicated that the $Na_2Mn_5O_{10}$ catalyst with 2×3 tunnel structure also permitted NO molecules with kinetic diameter of 0.317 nm enter the tunnel structure of $Na_2Mn_5O_{10}$. As is known, alkali metals exhibit strong NO adsorption capacity, and NO in the reaction system can be adsorbed by Na ions in the 2×3 tunnel structure of the $Na_2Mn_5O_{10}$ phase. At this point, lattice oxygen species on the inner surface of the tunnel structure would be reacted with NO to generate NO_2 , and then NO_2 diffused and oxidized soot particles to form CO_2 . The oxygen consumed from the inner surface of the tunnel structure is then replenished by oxygen species transferred from the Mn-O surface, further enhancing the reactivity and fluidity of oxygen species. For the above two reaction pathways, the two active sites, including Mn

and oxygen vacancies, contribute to the adsorption and activation of gaseous oxygen and NO. Meanwhile, the alkali metal ions in the $Na_2Mn_5O_{10}$ tunnel structure significantly improve the NO oxidation ability, and the formation of synergistic oxygen vacancies enhances the reactivity of oxygen species, thereby enhancing the catalytic activity of the $Na_2Mn_5O_{10}$ catalysts.

4. Conclusions

A series of romanechite-type $Na_2Mn_5O_{10}$ catalysts with a 2×3 tunnel structure were prepared via a facile hydrothermal method and utilized for the catalytic combustion of soot particles. The variations in hydrothermal reaction temperatures and Na:Mn molar ratios significantly impact the physico-chemical properties and catalytic performances of the $Na_xMn_yO_8$ catalysts. Among all the catalysts investigated in this study, the $Na_1Mn_2O_8$ -120 catalyst with a $Na_2Mn_5O_{10}$ phase exhibits the highest catalytic activity for soot combustion, with T_{10} , T_{50} , and T_{90} values of 281 °C, 317 °C, and 343 °C, respectively, which are considerably reduced to 271 °C, 310 °C, and 335 °C in the existence of 10% H_2O . According to the characterization results and DFT calculations results, the excellent catalytic performance of the $Na_2Mn_5O_{10}$ catalysts can be mainly attributed to their good reducibility, strong ability to adsorb and activate oxygen, and its ability to oxidize NO to NO_2 . These properties are observed for the $Na_2Mn_5O_{10}$ catalysts as their 2×3 tunnel structure has two active sites, Mn sites and oxygen vacancies, both of which are conducive to the adsorption and activation of O_2 and NO, providing favorable factors for the occurrence of the Langmuir-Hinshelwood (L-H) reaction pathway. Moreover, the alkali metal Na ions in the tunnel structure further enhance the adsorption of NO, and the consumption of lattice oxygen on the inner surface also promotes the mobility and reactivity of oxygen species. Moreover, the romanechite-type $Na_2Mn_5O_{10}$ catalysts possess extremely high stability and excellent water and sulfur resistance during the soot oxidation reaction. Considering the convenient synthesis, low cost, and high catalytic performance of the $Na_2Mn_5O_{10}$ catalysts, the present research study provides promising materials for diesel soot combustion.

CRediT authorship contribution statement

Wang Lanyi: Data curation, Formal analysis, Visualization. **Zhang Chunlei:** Data curation, Formal analysis, Investigation, Methodology. **Peng Chao:** Data curation, Formal analysis, Investigation, Methodology. **Ren Yu:** Data curation, Formal analysis, Investigation, Visualization. **Yu Di:** Data curation, Formal analysis, Investigation, Methodology, Writing – original draft. **Yu Xuehua:** Data curation, Formal analysis, Funding acquisition, Investigation, Methodology, Project administration, Writing – review & editing. **Zhao Zhen:** Conceptualization, Funding acquisition, Project administration, Resources, Supervision, Validation, Writing – review & editing. **Fan Xiaoqiang:** Data curation, Formal analysis, Investigation.

Declaration of Competing Interest

The authors declare that they have no known competing financial interests or personal relationships that could have appeared to influence the work reported in this paper.

Data availability

The authors do not have permission to share data.

Acknowledgements

This work was supported by National Natural Science Foundation of China (U1908204, 22072095, 22372107); National Key R&D Program of China (2022YFB3506200, 2022YFB3504100); Excellent Youth

Science Foundation of Liaoning Province (2022-YQ-20); Shenyang Science and Technology Planning Project (22-322-3-28); Liaoning Xingliao talented youth Top talent program; University Joint Education Project for China-Central and Eastern European Countries (2021097).

Appendix A. Supporting information

Supplementary data associated with this article can be found in the online version at doi:10.1016/j.apcatb.2023.123614.

References

- [1] R. Kimura, J. Wakabayashi, S.P. Elangovan, M. Ogura, T. Okubo, Nepheline from K_2CO_3 /nanosized sodalite as a prospective candidate for diesel soot combustion, *J. Am. Chem. Soc.* 130 (2008) 12844–12845.
- [2] C. Cao, L. Xing, Y. Yang, Y. Tian, T. Ding, J. Zhang, T. Hu, L. Zheng, X. Li, Diesel Soot elimination over potassium-promoted Co_3O_4 nanowires monolithic catalysts under gravitation contact mode, *Appl. Catal. B: Environ.* 218 (2017) 32–45.
- [3] B. Frank, M.E. Schuster, R. Schlögl, D.S. Su, Emission of highly activated soot particulate - the other side of the coin with modern diesel engines, *Angew. Chem. Int. Ed.* 52 (2013) 2673–2677.
- [4] Y. Wei, Y. Zhang, P. Zhang, J. Xiong, X. Mei, Q. Yu, Z. Zhao, J. Liu, Boosting the removal of diesel soot particles by the optimal exposed crystal facet of CeO_2 in Au/ CeO_2 catalysts, *Environ. Sci. Technol.* 54 (2020) 2002–2011.
- [5] Y. Wei, P. Zhang, J. Xiong, Q. Yu, Q. Wu, Z. Zhao, J. Liu, SO₂-tolerant catalytic removal of soot particles over 3D ordered macroporous Al_2O_3 -supported binary Pt–Co oxide catalysts, *Environ. Sci. Technol.* 54 (2020) 6947–6956.
- [6] J. Xiong, X. Mei, J. Liu, Y. Wei, Z. Zhao, Z. Xie, J. Li, Efficiently multifunctional catalysts of 3D ordered meso-macroporous $Ce_{0.3}Zr_{0.7}O_2$ -supported PdAu@ CeO_2 core-shell nanoparticles for soot oxidation: Synergistic effect of Pd-Au- CeO_2 ternary components, *Appl. Catal. B: Environ.* 251 (2019) 247–260.
- [7] M. Wang, Y. Zhang, Y. Yu, W. Shan, H. He, Cesium as a dual function promoter in $Co/Ce-Sn$ catalyst for soot oxidation, *Appl. Catal. B: Environ.* 285 (2021), 119850.
- [8] D. Jampaiah, V.K. Velisjou, P. Venkataswamy, V.E. Coyle, A. Nafady, B.M. Reddy, S.K. Bhargava, Nanowire morphology of mono- and bidoped α - MnO_2 catalysts for remarkable enhancement in soot oxidation, *ACS Appl. Mater. Interfaces* 9 (2017) 32652–32666.
- [9] D. Yu, Y. Ren, X. Yu, X. Fan, L. Wang, R. Wang, Z. Zhao, K. Cheng, Y. Chen, Z. Sojka, A. Kotarba, Y. Wei, J. Liu, Facile synthesis of birnessite-type $K_2Mn_4O_8$ and cryptomelane-type $K_{2-x}Mn_8O_{16}$ catalysts and their excellent catalytic performance for soot combustion with high resistance to H_2O and SO_2 , *Appl. Catal. B: Environ.* 285 (2021), 119779.
- [10] M. Fedyna, P. Legutko, J. Grybos, J. Janas, X. Yu, Z. Zhao, A. Kotarba, Z. Sojka, Screening investigations into the effect of cryptomelane doping with 3d transition metal cations on the catalytic activity in soot oxidation, NO_2 formation and SO_2 resistance, *Appl. Catal. A: Gen.* 624 (2021), 118302.
- [11] X. Chen, Y.F. Shen, S.L. Suib, C.L. O'Young, Characterization of manganese oxide octahedral molecular sieve (M-OMS-2) materials with different metal cation dopants, *Chem. Mater.* 14 (2002) 940–948.
- [12] W. Hong, T. Zhu, Y. Sun, H. Wang, X. Li, F. Shen, Enhancing oxygen vacancies by introducing Na^+ into OMS-2 tunnels to promote catalytic ozone decomposition, *Environ. Sci. Technol.* 53 (2019) 13332–13343.
- [13] J. Grybos, M. Fedyna, P. Legutko, B. Leszczynski, J. Janas, A. Wach, J. Szlachetko, X. Yu, A. Kotarba, Z. Zhao, Z. Sojka, Mechanistic insights into oxygen dynamics in soot combustion over cryptomelane catalysts in tight and loose contact modes via $^{18}O_2/^{16}O_2$ isotopic variable composition measurements-a hot ring model of the catalyst operation, *ACS Catal.* 11 (2021) 9530–9546.
- [14] C. Peng, D. Yu, C. Zhang, M. Chen, L. Wang, X. Yu, X. Fan, Z. Zhao, K. Cheng, Y. Chen, Y. Wei, J. Liu, Alkali/alkaline-earth metal-modified MnO_x supported on three-dimensionally ordered macroporous–mesoporous $Ti_xSi_{1-x}O_2$ catalysts: Preparation and catalytic performance for soot combustion, *J. Environ. Sci.* 125 (2023) 82–94.
- [15] H. Xu, N. Yan, Z. Qu, W. Liu, J. Mei, W. Huang, S. Zhao, Gaseous heterogeneous catalytic reactions over Mn-based oxides for environmental applications: A critical review, *Environ. Sci. Technol.* 51 (2017) 8879–8892.
- [16] J. Luo, Q. Zhang, J. Garcia-martinez, S.L. Suib, Adsorptive and acidic properties, reversible lattice oxygen evolution, and catalytic mechanism of cryptomelane-type manganese oxides as oxidation catalysts, *J. Am. Chem. Soc.* 130 (2008) 3198–3207.
- [17] G. Kresse, J. Furthmüller, Efficiency of ab-initio total energy calculations for metals and semiconductors using a plane-wave basis set, *Comp. Mater. Sci.* 6 (1996) 15–50.
- [18] G. Kresse, D. Joubert, From ultrasoft pseudopotentials to the projector augmented-wave method, *Phys. Rev. B* 59 (1999) 1758.
- [19] J.P. Perdew, K. Burke, M. Ernzerhof, Generalized gradient approximation made simple, *Phys. Rev. Lett.* 77 (1996) 3865.
- [20] P.E. Blöchl, Projector augmented-wave method, *Phys. Rev. B* 50 (1994) 17953.
- [21] E. Cockayne, L. Li, First-principles DFT+U studies of the atomic, electronic, and magnetic structure of α - MnO_2 (cryptomelane), *Chem. Phys. Lett.* 544 (2012) 53–58.
- [22] S. Grimme, J. Antony, S. Ehrlich, H. Krieg, A consistent and accurate ab initio parametrization of density functional dispersion correction (DFT-D) for the 94 elements H–Pu, *J. Chem. Phys.* 132 (2010), 154104.
- [23] S. Grimme, Semiempirical GGA-type density functional constructed with a long-range dispersion correction, *J. Comput. Chem.* 27 (2006) 1787–1799.
- [24] H.J. Monkhorst, J.D. Pack, Special points for Brillouin-zone integrations, *Phys. Rev. B* 13 (1976) 5188–5192.
- [25] Y. Xie, P. Li, Y. Zeng, X. Li, Y. Xiao, Y. Wang, Y. Zhang, Thermally treated fungal manganese oxides for bisphenol A degradation using sulfate radicals, *Chem. Eng. J.* 335 (2018) 728–736.
- [26] S. Liu, C. Fan, Y. Zhang, C. Li, X. You, Low-temperature synthesis of $Na_2Mn_5O_{10}$ for supercapacitor applications, *J. Power Sources* 196 (2011) 10502–10506.
- [27] X. Shen, Y. Ding, J. Liu, K. Laubernd, R.P. Zerger, M. Polverejan, Y. Son, M. Aindow, S.L. Suib, Synthesis, characterization, and catalytic applications of manganese oxide octahedral molecular sieve (OMS) nanowires with a 2 × 3 tunnel structure, *Chem. Mater.* 16 (2004) 5327–5335.
- [28] E. Adamczyk, V. Pralong, $Na_2Mn_5O_{10}$: a suitable electrode material for Na-ion batteries? *Chem. Mater.* 29 (2017) 4645–4648.
- [29] C. Kuo, I.M. Mosa, A.S. Poyraz, S. Biswas, A.M. El-Sawy, W. Song, Z. Luo, S. Chen, J.F. Rusling, J. He, S.L. Suib, Robust mesoporous manganese oxide catalysts for water oxidation, *ACS Catal.* 5 (2015) 1693–1699.
- [30] K. Ramesh, L. Chen, F. Chen, Z. Zhong, J. Chin, H. Mook, Y. Han, Preparation and characterization of coral-like nanostructured α - Mn_2O_3 catalyst for catalytic combustion of methane, *Catal. Commun.* 8 (2007) 1421–1426.
- [31] R. Baddour-Hadjean, J.P. Pereira-Ramos, Raman microspectrometry applied to the study of electrode materials for lithium batteries, *Chem. Rev.* 110 (2009) 1278–1319.
- [32] J.E. Post, D.A. McKeown, P.J. Heaney, Raman spectroscopy study of manganese oxides: tunnel structures, *Am. Mineral.* 105 (2020) 1175–1190.
- [33] A. Ramírez, P. Hillebrand, D. Stellmach, M. May, P. Bogdanoff, S. Fiechter, Evaluation of MnO_x , Mn_2O_3 , and Mn_3O_4 electrodeposited films for the oxygen evolution reaction of water, *J. Phys. Chem. C* 118 (2014) 14073–14081.
- [34] Q. Yu, J. Xiong, Z. Li, X. Mei, P. Zhang, Y. Zhang, Y. Wei, Z. Zhao, J. Liu, Optimal exposed crystal facets of α - Mn_2O_3 catalysts with enhancing catalytic performance for soot combustion, *Catal. Today* 376 (2021) 229–238.
- [35] H. Deng, S. Kang, J. Ma, C. Zhang, H. He, Silver incorporated into cryptomelane-type manganese oxide boosts the catalytic oxidation of benzene, *Appl. Catal. B: Environ.* 239 (2018) 214–222.
- [36] H. Deng, S. Kang, J. Ma, L. Wang, C. Zhang, H. He, Role of structural defects in MnO_x promoted by Ag doping in the catalytic combustion of volatile organic compounds and ambient decomposition of O_3 , *Environ. Sci. Technol.* 53 (2019) 10871–10879.
- [37] M. Hu, K. Zhou, T. Zhao, Z. Li, X. Zeng, D. Yu, X. Yu, M. Zhao, Z. Shao, Q. Xu, B. Cui, Facile preparation and efficient $MnxCoy$ porous nanosheets for the sustainable catalytic process of soot, *Green. Energy Environ.* (2023).
- [38] Z. Huo, P. Zhao, P. Miu, L. Ren, B. Tan, N. Feng, H. Wan, G. Guan, Enhanced catalytic oxidation of soot over 3DOM $LaMnO_3$ by adding Ag and CeO_2 : Improving the generation and delivery of active oxygen species, *Appl. Surf. Sci.* 600 (2022), 154204.
- [39] S. Liu, X. Wu, D. Weng, M. Li, R. Ran, Roles of acid sites on Pt/H-ZSM5 catalyst in catalytic oxidation of diesel soot, *ACS Catal.* 5 (2015) 909–919.
- [40] L. Chen, Y. Liu, X. Fang, Y. Cheng, Simple strategy for the construction of oxygen vacancies on α - MnO_2 catalyst to improve toluene catalytic oxidation, *J. Hazard. Mater.* 409 (2021), 125020.
- [41] L. Dai, Y. Wang, L. Sun, Y. Ding, Y. Yao, L. Yao, N.E. Drewett, W. Zhang, J. Tang, W. Zheng, Jahn-teller distortion induced Mn^{2+} -rich cathode enables optimal flexible aqueous high-voltage Zn-Mn batteries, *Adv. Sci.* 8 (2021) 2004995.
- [42] J. Yao, Y. Liu, Y. Li, J. Jiang, Q. Zhu, Facile synthesis of Mn_2O_3/Mn_3O_4 composites with superior zinc ion storage performance, *Mater. Res. Bull.* 165 (2023), 112292.
- [43] L. Xing, Y. Yang, C. Cao, D. Zhao, Z. Gao, W. Ren, Y. Tian, T. Ding, X. Li, Decorating CeO_2 nanoparticles on Mn_2O_3 nanosheets to improve catalytic soot combustion, *ACS Sustain. Chem. Eng.* 6 (2018) 16544–16554.
- [44] Y. Yang, D. Zhao, Z. Gao, Y. Tian, T. Ding, J. Zhang, Z. Jiang, X. Li, Interface interaction induced oxygen activation of cactus-like Co_3O_4 /OMS-2 nanorod catalysts in situ grown on monolithic cordierite for diesel soot combustion, *Appl. Catal. B: Environ.* 286 (2021), 119932.
- [45] H. Deng, S. Kang, J. Ma, C. Zhang, H. He, Silver incorporated into cryptomelane-type manganese oxide boosts the catalytic oxidation of benzene, *Appl. Catal. B: Environ.* 239 (2018) 214–222.
- [46] C. Calvert, R. Roesten, K. Ngala, J. Villegas, A. Morey, X. Shen, S.L. Suib, Synthesis, characterization, and rietveld refinement of tungsten-framework-doped porous manganese oxide (K-OMS-2) material, *Chem. Mater.* 20 (2008) 6382–6388.
- [47] C. Peng, Y. Ren, D. Yu, L. Wang, C. Zhang, X. Fan, X. Yu, Z. Zhao, Y. Wei, J. Liu, K-modified MnO_x catalysts with tunnel structure and layered structure: Facile preparation and catalytic performance for soot combustion, *Nano Res.* 16 (2023) 6187–6199.
- [48] W. Ren, T. Ding, Y.X. Yang, L.L. Xing, Q.P. Cheng, D.Y. Zhao, Z.L. Zhang, Q. Li, J. Zhang, L.R. Zheng, Identifying oxygen activation/oxidation sites for efficient soot combustion over silver Catalysts interacted with nanoflower-like hydroxylcitederived $CoAlO$ metal oxides, *ACS Catal.* 9 (2019) 8772–8784.
- [49] D. Yu, X. Yu, C. Zhang, L. Wang, X. Fan, Z. Zhao, Y. Wei, J. Liu, J. Grybos, B. Leszczynski, A. Wach, D. Wierzbicki, A. Kotarba, Z. Sojka, Layered $Na_2Mn_5O_{10}$ decorated by Cerium as the robust catalysts for efficient low temperature soot combustion, *Appl. Catal. B: Environ.* 338 (2023), 123022.

[50] J. Ma, M. Mahmoodinia, K.R. Rout, E.A. Blekkan, High-temperature sulfur capture by a Mn-Mo sorbent: an investigation of regeneration conditions and SO₂ formation and prevention, *Chem. Eng. Sci.* 274 (2023), 118674.

[51] J. Wang, Z. Nie, Z. An, H. Bai, F. Wang, X. Zhang, Y. Li, C. Wang, Improvement of SO₂ resistance of low-temperature Mn-based denitrification catalysts by Fe doping, *ACS Omega* 4 (2019) 3755–3760.

[52] X.H. Yu, Y. Ren, D. Yu, M.Z. Chen, L.Y. Wang, R.D. Wang, X.Q. Fan, Z. Zhao, K. Cheng, Y.S. Chen, J. Grybóś, A. Kotarba, Z. Sojka, Y.C. Wei, J. Liu, Hierarchical porous K-OMS-2/3DOM-m Ti_{0.7}Si_{0.3}O₂ catalysts for soot combustion: easy preparation, high catalytic activity, and resistance to H₂O and SO₂, *ACS Catal.* 11 (2021) 5554–5571.

[53] Z. Zhang, D. Han, S. Wei, Y. Zhang, Determination of active site densities and mechanisms for soot combustion, *J. Catal.* 276 (2010) 16–23.

[54] S. Jian, Y. Yang, W. Ren, L. Xing, D. Zhao, Y. Tian, T. Ding, X. Li, Kinetic analysis of morphologies and crystal planes of nanostructured CeO₂ catalysts on soot oxidation, *Chem. Eng. Sci.* 226 (2020), 115891.

[55] H. Hu, S. Cai, H. Li, L. Huang, L. Shi, D. Zhang, In situ DRIFT's investigation of the low-temperature reaction mechanism over Mn-doped Co₃O₄ for the selective catalytic reduction of NO_x with NH₃, *J. Phys. Chem. C.* 119 (2015) 22924–22933.

[56] L. Chen, J. Li, M. Ge, DRIFT study on cerium–tungsten/titania catalyst for selective catalytic reduction of NO_x with NH₃, *Environ. Sci. Technol.* 44 (2010) 9590–9596.

[57] Z. Li, M. Meng, Y. Zha, F. Dai, T. Hu, Y. Xie, J. Zhang, Highly efficient multifunctional dually-substituted perovskite catalysts La_{1-x}K_xCo_{1-y}Cu_yO_{3-δ} used for soot combustion, NO_x storage and simultaneous NO_x-soot removal, *Appl. Catal. B: Environ.* 121 (2012) 65–74.

[58] X.G. Li, Y.H. Dong, H. Xian, W. Hernández, M. Meng, H.H. Zou, A.J. Ma, T. Y. Zhang, Z. Jiang, N. Tsubaki, P. Vernoux, De-NO_x in alternative lean/rich atmosphere on La_{1-x}Sr_xCoO₃ perovskites, *Energy Environ. Sci.* 4 (2011) 3351–3354.

[59] L. Zhang, L. Shi, L. Huang, J. Zhang, R. Gao, D. Zhang, Rational design of high-performance DeNO_x catalysts based on Mn_xCo_{3-x}O₄ nanocages derived from metal–organic frameworks, *ACS Catal.* 4 (2014) 1753–1763.

[60] N.D. Wasalathantri, T.M. SantaMaria, D.A. Kriz, S.L. Dissanayake, C. Kuo, S. Biswas, S.L. Suib, Mesoporous manganese oxides for NO₂ assisted catalytic soot oxidation, *Appl. Catal. B: Environ.* 201 (2017) 543–551.

[61] Z.M. Wang, S. Tezuka, H. Kanoh, Characterization of the structural and surface properties of a synthesized hydrous hollandite by gaseous molecular adsorption, *Chem. Mater.* 13 (2001) 530–537.